1
Computational Viscoelastic Fluid Mechanics and Numerical Studies of Turbulent Flows of Dilute Polymer Solutions

Antony N. Beris and Kostas D. Housiadas

1.1
Introduction and Historical Perspective

According to the late A.B. Metzner [1], the phenomenon of polymer-induced drag reduction was independently discovered by two researchers, K.J. Mysels in May 1945, as reported by the discoverer at an AIChE symposium on drag reduction in 1970, and B.A. Toms in the summer of 1945, as reported by the discoverer at the IUTAM symposium on the structure of turbulence and drag reduction held in Washington, DC in 1976. The original fluids studied in these two first experimental investigations were micellar aluminum disoaps or rubber in gasoline (K.J. Mysels) and polymethyl methacrylate in monochlorobenzene (B.A. Toms). However, due to the war, the first records in an accessible publication were found later [2, 3] with journal contributions even much later [4, 5]. Since that time, the field has literally exploded with 500 papers until the seminal review by Virk [6] and 4900 papers by 1995 [1].

The first attribution of drag reduction to fluid viscoelasticity was by Dodge and Metzner [7], whereas the first description of drag reduction as "Toms effect" was by Fabula at the Fourth International Congress on Rheology, held in 1996 [8]. The first measurements of viscoelasticity of drag-reducing fluids were performed by Metzner and Park [9] and Hershey and Zakin [10]. The first articulations of a "maximum drag reduction asymptote" for dilute polymer solutions were reported by Castro and Squire [11], Giles and Pettit [12], and Virk *et al.* [13]. As far as the first proposed mechanisms of drag reduction due to fluid mechanical effects are concerned, Lumley attributed drag reduction to molecular stretching in the radial flow patterns in turbulent flows [14]. Simultaneously, Seyer and Metzner [15] clarified it even further, as due to high extensional deformation rates in radial flow patterns in turbulent flows and high resistance to stretching of viscoelastic fluids. More recently, Lumley and Blossey [16] elaborated further by arguing that polymer additives, by boosting the extensional viscosity of the fluid, affect especially the structure of the turbulent bursts; see also Ref. [17]. This same mechanism is also suspected to be operative when other additives are employed, such as micellar surfactant solutions [2, 4, 18–20]

Modeling and Simulation in Polymers. Edited by P.D. Gujrati and A.I. Leonov

ISBN: 978-3-527-32415-6

and fiber suspensions [21]. Ever since Virk [6] made the first thorough review of drag reduction, the interest in the phenomenon continues uninterrupted – see, for example, the experimental works [22–26], the more recent reviews by Sellin and Moses [27, 28] and Bushnell and Hefner [29], the book by Gyr and Bewersdorff [30], and the latest reviews by Nieuwstadt and Den Toonder [31], Graham [32], and White and Mungal [33].

The phenomenon of polymer-induced drag reduction [5, 6, 34, 35] describes the effect of relatively small quantities, as small as on the order of ppm by weight, of a high molecular weight polymer, which when added to a low molecular weight solvent, such as water or crude oil, reduce the turbulent drag; see Figure 1.1 for a representation of some early but standard experimental results as adapted from Virk [6]. According to Metzner [1], Lummus *et al.* [36] recorded what appears to be the first commercial exploitation of turbulent drag reduction, using polymeric additives to increase oil well drilling rates in 50 wells in the United States and Canada. Increases in drilling rate were tabulated. The first publicly recorded usage of drag reduction in pipelines appears to be that of Burger *et al.* [37], who reported results for 1 and 2 in.

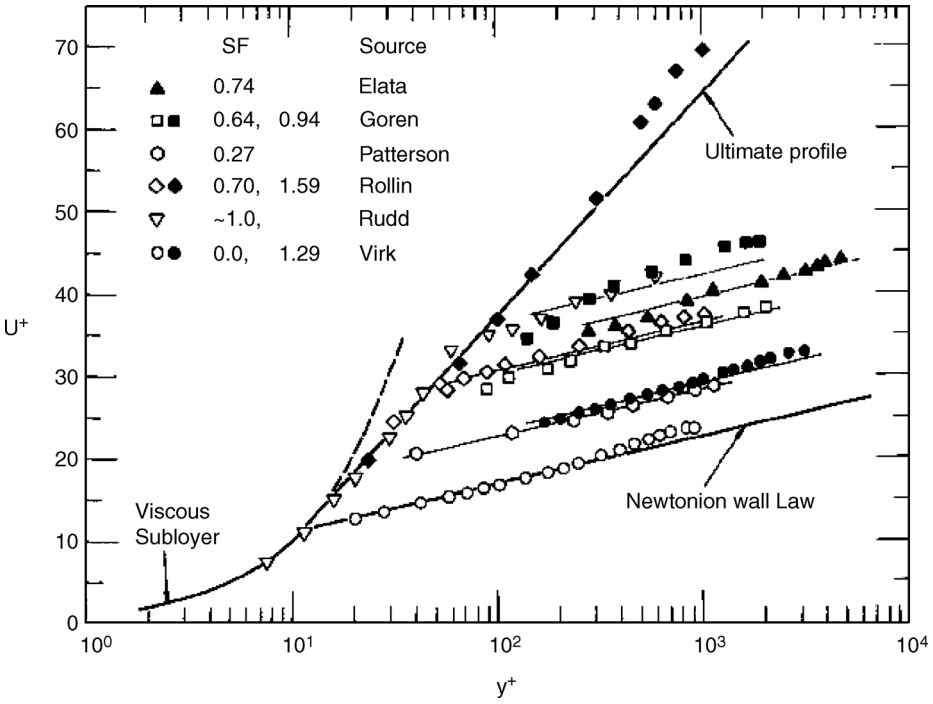

Figure 1.1 Velocity profiles in flows with drag reduction. The different symbols represent different polymer solutions; the open circles provide the pure solvent (water) base data. As polymer additives are introduced, and for the same pressure drop (equivalently, the same wall stress, i.e., the same velocity slope at the wall), the flow rate increases, from the base line to the maximum (Virk) asymptote, called "Ultimate Profile" in the figure [6]. (Reprinted with permission from John Wiley & Sons)

tubes as well as 14 and 48 in. pipelines. The best available estimates of usage in petroleum transportation in 2004, obtained from industry sources, state that drag reducers are employed to treat approximately 20 million barrels of hydrocarbons per day, which may be compared with a worldwide crude oil production rate of about 80 million bpd. A major application is in facilitating the oil transfer through the Alaskan pipeline [38]. Commercial-scale tests of drag-reducing additives in municipal heating and cooling systems are described by Zakin *et al.* [18], with emphasis on surfactant additives – there is also a reference to an application to the heating system of pipelines in offshore drilling [20]. It is interesting to note that the drag reductions achieved by using surfactant (colloidal) additives are very large and may exceed those of the "maximum drag-reducing asymptote" for dilute polymer solutions, as is also the case when fiber–polymer mixtures are employed [39]. We are unaware of any regular commercial use of these materials. Incidentally, marine applications of turbulent drag reduction have been studied for many decades and measurements performed of dilute solutions of fish mucus that is polymeric in nature in turbulent pipe flow exhibited as much as 66% reduction in friction drag [40]. Even snails were found to produce a mucus that reduces drag [40].

During the past 15 years, the most significant progress undoubtedly came in the theoretical front from the development of direct numerical simulations (DNS) due to advances in computational viscoelastic fluid mechanics, models, methods, and computer hardware (parallel computing). The goal was to theoretically understand in more depth the nature and the underlying mechanisms of polymer-induced drag reduction. The simulations, with the exception of some limited work on homogeneous viscoelastic turbulence [41], have primarily focused on the analysis of inhomogeneous turbulent viscoelastic flows. Even there, with the exception of some limited work on boundary layer flows [42, 43] – see also the very recent review by White and Mungal [33] – and pipe flow [44], the bulk of the work has focused on simulations of channel flow. The very first simulations (those reported by Orlandi [45] and Den Toonder *et al.* [44]) used ad hoc constitutive relationships for the stress that attempted to empirically capture the increase in the resistance to extensional deformation so characteristic to polymeric systems. As a result, they did get some encouraging results, exhibiting the right trends with increasing viscoelasticity in the flow, in agreement with experimental observations [23, 30, 44]. For example, they noticed a decrease in the strength of longitudinal structures accompanied by an increase in their spacing with increasing polymer concentration [45] and drag reduction with the right changes in the root mean square (rms) values of the velocity fluctuations and velocity probability distribution functions (pdf), exhibiting increasing intermittency [44].

However, the first DNS based on a microscopically originated constitutive equation for the polymer dynamics (the finite extensibility nonlinear elastic with the Peterlin approximation (FENE-P) model [46]) was conducted by Sureshkumar *et al.* [47]. In this work, for a fixed friction Reynolds number and other rheological parameters, drag reduction was observed as the Weissenberg number increased beyond a critical onset value. Moreover, accompanying drag reduction, characteristic changes were observed in the velocity and vorticity mean and rms values, the Reynolds stress, and

the energy spectra all in qualitative agreement with experimental observations obtained with drag-reducing dilute polymer solutions [22, 23, 48]. Shortly afterward, DNS based on a network-based constitutive model, the Giesekus model [49], also produced similar results [50]. These large-scale (three-dimensional and time-dependent) simulations under turbulent conditions are similar to the ones carried out for Newtonian fluids [51, 52] and also account for the presence of the polymer additives through a full modeling of the coupled effect of additives on the flow.

Since these initial works, we have seen a flourishing of DNS works by our own [53–58] and many other [59–66] research groups. We include in the discussion here only those works that involve the fully coupled flow and polymer concentration problem; there are many more works that monitored the polymer molecular extension against a fixed flow field obtained from Newtonian DNS (see, for example, Ref. [67]) – this is a much simpler computational problem, many of the numerical stability problems emerge only when the fully coupled problem is considered. Of interest is the spectral DNS work by De Angelis *et al.* [59] showing as main effect of viscoelasticity a quite concentrated action on bursting phenomena and a stabilization of the streaks resulting in fewer, bigger, coherent structures, reinforcing previous results [47]. Later work [60] involving the application of a Karhunen–Loéve (K-L) decomposition for the extraction of information on larger coherent structures in the flow (following Refs [68–70] and others) has reported that the main change in viscoelasticity is primarily an energy redistribution among the K-L modes, while the spatial profile of the most energetic modes stays the same. This is in contrast to the findings in Ref. [58] where a similar K-L decomposition has also revealed substantial changes in the spatial structure of the most energetic modes and an overall enhancement of the energy content of the first few modes of the decomposition upon addition of viscoelasticity. However, this may be just due to the higher elasticity of flows in direct numerical simulations in Ref. [58] allowing to more clearly see these effects.

Another work worth mentioning as a measure of the activity in the field is that of Ptasinski *et al.* [62]. The authors in this work asserted that they have simulated cases close to maximum drag reduction by using model parameters (such as a high Weissenberg number, 50, a high extensibility parameter value, 33, and, primarily, a small solvent to total viscosity ratio, of order 0.5) implying a high polymer contribution. The results indeed seem to be in agreement with expectations (such as a law-of-the-wall with a significantly high slope) with drag reductions on the order of 60–65% for the higher elasticity cases. However, there still remain questions primarily due to the small computational domain size used (minimal channel of $(3 \times 2 \times 2)$ made dimensionless by the half channel-height and small mesh resolution of $(48 \times 32 \times 100)$ in the x, y, and z directions, respectively, along with mixed spectral (along the period directions, x and y) and finite difference (along the wall-normal direction, z) approximations). Given the fact that, as mentioned above, one dominant effect of viscoelasticity is to lead to substantially larger organized coherent structures than those seen in Newtonian flows, the use of this minimal computational domain size places questions on the validity of the final results. Even more questions are placed based on the small mesh resolution used, especially along the shear direction. For the Reynolds number used (friction Reynolds number of 180), a

mesh size of at least 96 ought to have been used. Moreover, the technique used was not immune to flow instabilities (as also the standard spectral method), and an extra conformation diffusion was also needed to be used (let alone the diffusion introduced by the use of the finite difference approximation along the sheatwise (z) direction). So, although progress is definitely made, still there are questions regarding the validity of this and other maximum drag reduction results that make that state still, in our opinion, unsolved. To achieve a solution in this regime is a very demanding task both from a computational perspective and from a polymer modeling perspective.

Other works used, instead of spectral, lower order accuracy finite difference approximations, but they have to be noted here since they employed more suitable numerical formulations for the constitutive equations that explicitly avoided the introduction of artificial diffusivity in the numerical solution [61, 63–66]. Those works also employed the FENE-P model to simulate dilute polymer solutions [61, 63, 64] or the Giesekus model for surfactant turbulent flow [19, 65, 66].

Moreover, we have recently seen, in addition to straight DNS computations, some very substantial theoretical analyses, as very elegant analyses based on the examination of exact coherent states in plane shear flow, by Stone *et al.* [71]. These represent unstable solutions of the laminar flow problem in terms of traveling waves – see also the excellent review by Graham [32]. The analysis of the effects of viscoelasticity on these states has shown [72] that they mirrored the changes observed in experiments and simulations of fully turbulent flows of polymer solutions: this similarity establishes again the importance of large-scale structures in turbulent flow. Their modification by viscoelasticity elegantly reveals most of the drag-reducing effects. This work followed a similar analysis performed only relatively recently for Newtonian turbulent flows [73]. An exciting development was also the recent experimental discovery of the dominant traveling wave mode in a Newtonian turbulent pipe flow field [74] indicating the physical significance in further theoretical investigations of large coherent motion structures in turbulent flows. These results are also consistent with other methods of analysis of large-scale coherent motion such as the K-L decomposition ([68–70] and references therein). As already mentioned, K-L analysis of viscoelastic turbulent channel flow has also been conducted by de Angelis *et al.* [60], Housiadas *et al.* [58], and, more recently, by Handler *et al.* [75] and Samanta *et al.* [76], indicating a significant enhancement of the energy contained in the large scales as viscoelasticity sets in. The relevance of these results in improving our understanding makes these types of analyses highly desirable in future work, along with more traditional analysis of the turbulence statistics. In parallel, there is considerable recent work, taking sometimes advantage of the insight developed thanks to DNS results, aimed at developing $\kappa-\varepsilon$-type turbulent models applicable for drag-reducing polymer flows – see, for example, Refs [17, 77] and references therein. However, due to space limitations, we will not discuss any further these and related investigations.

This chapter aims to present, in a concise way, the major elements and results from applications of computational viscoelastic fluid mechanics in numerical studies (DNS) of turbulent channel flows of homogeneous, dilute, polymer solutions under drag-reducing conditions. In the next section, we present a summary and outline of governing equations with emphasis on polymer modeling. In Section 1.3, we

describe key elements of the spectral method algorithm as the principal numerical method used in DNS investigations. Section 1.4 overviews the main results of the DNS with an emphasis on the principal effects of the variation of key dimensionless numbers and rheological characteristics on the most important turbulent statistics. A discussion on the influence of numerical parameters is also included. Finally, Section 1.5 contains the conclusions and some thoughts for future work.

1.2 Governing Equations and Polymer Modeling

The first among the governing equations used in DNS are the mass and momentum balances, which for an incompressible, isothermal, and constant polymer concentration flow in a channel are given in dimensionless form as

$$\underline{\nabla} \cdot \underline{u} = 0, \tag{1.1}$$

$$\frac{\mathrm{D}\underline{u}}{\mathrm{D}t} = -\underline{\nabla} p + \frac{\beta_0}{Re_{\tau 0}} \underline{\nabla}^2 \underline{u} + \frac{1-\beta_0}{Re_{\tau 0}} \underline{\nabla} \cdot \underline{\underline{\tau}} + \underline{e}_x, \tag{1.2}$$

where $\mathrm{D}/\mathrm{D}t \equiv (\partial/\partial t) + \underline{u} \cdot \underline{\nabla}$ denotes the material derivative, $\beta_0 \equiv (\eta_s^*/\eta_0^*) = (\eta_s^*/(\eta_s^* + \eta_{p0}^*))$ is the ratio of the solvent viscosity η_s^* to the total zero shear rate viscosity of the solution η_0^*, and $Re_{\tau 0}$ is the zero shear rate friction Reynolds number, $Re_{\tau 0} \equiv (u_\tau^* h^*/\nu_0^*)$, where u_τ^* is the friction velocity defined as $u_\tau^* \equiv \sqrt{\tau_w^*/\varrho^*}$, where τ_w^* is the total wall shear stress and ϱ^* is the constant density of the solution, h^* is the half channel width, and $\nu_0^* \equiv (\eta_0^*/\varrho^*)$ is the zero shear rate kinematic viscosity of the solution. In Eqs. (1.1) and (1.2), $\underline{u} = u_x \underline{e}_x + u_y \underline{e}_y + u_z \underline{e}_z$ is the (dimensionless) velocity vector, where $\underline{e}_x, \underline{e}_y, \underline{e}_z$ are the unit vectors along the axes, p is the (dimensionless) periodic part of the pressure, and $\underline{\underline{\tau}}$ is the (dimensionless) extra stress tensor, introduced due to the presence of polymer in the flow. The momentum balance, Eq. (1.2), has been formulated for pressure-driven flow along the streamwise direction x, and this is how the constant term $\underline{e}_x$ arises. Equations (1.1) and (1.2) have been nondimensionalized by using the characteristic scales reported in the first column in Table 1.1, usually referred to as "computational scales," as opposed to the "zero shear rate wall scales" and the "actual wall scales" reported in columns 2 and 3, respectively. In Table 1.1, u_b^* is the average (bulk) velocity, η_{p0}^* is the zero shear rate polymer viscosity, k_B^* is the Boltzmann constant, T^* is the absolute temperature, and K^* is the characteristic elastic spring strength of the nonlinear elastic dumbbell. Note that the superscript asterisk denotes a dimensional quantity. More details can be found in Ref. [78].

Note that in viscoelastic turbulent flows, because of the shear thinning effect [35, 79], we have to distinguish between two different types of wall units. One is based on the zero shear properties and the other, applicable for channel and boundary layer

Table 1.1 Characteristic computational and wall scales for fixed wall stress except for the last column that is for fixed flux conditions.

Quantity	Computational scale	Reference wall scale	Actual wall scale	Computational scale (fixed flux)
Length	h^*	ν_0^*/u_τ^*	ν^*/u_τ^*	h^*
Velocity	u_τ^*	u_τ^*	u_τ^*	u_b^*
Time	h^*/u_τ^*	ν_0^*/u_τ^{*2}	ν^*/u_τ^{*2}	h^*/u_b^*
Pressure	τ_w^*	τ_w^*	τ_w^*	$\varrho^* u_b^{*2}$
Polymer stress	$\eta_{p0}^* u_\tau^*/h^*$	$\eta_{p0}^* u_\tau^{*2}/\nu_0^*$	$\eta_{p0}^* u_\tau^{*2}/\nu^*$	$\eta_{p0}^* u_b^*/h^*$
Conformation	$k_B^* T^*/K^*$	$k_B^* T^*/K^*$	$k_B^* T^*/K^*$	$k_B^* T^*/K^*$

flows, on the stationary wall conditions [78]. The advantage of the first is that it gives rise to quantities that are a priori known so that it makes easier the setting up of numerical computations. In fact, in practice, the numerical simulations are set only in terms of such nondimensionalization. However, because of shear thinning, the actual viscous shear viscosity next to the wall is different from its zero shear rate value. As a result, the proportionality of the velocity and the distance that it is expected to hold in the viscous sublayer next to the wall, when both are expressed in terms of wall units, $u^+ = y^+$ [34], no longer holds when the zero shear rate viscosity is used to scale the length distance. Therefore, to allow a physical interpretation of the results, it is necessary to use the actual wall viscosity value in order to construct the dimensionless wall length and time units. However, a disadvantage of this approach is that since with viscoelastic systems the total shear viscosity is not a material property but essentially an "effective" quantity that can be determined only a posteriori after the full solution is known, such nondimensionalization can also be performed only a posteriori. For dilute solutions, since the bulk of the solution shear viscosity is due to the solvent and stays constant, we only have small changes due to this rescaling from zero shear rate (nominal) to the actual wall values. Moreover, as DNS information indicates [78], the correction can be approximated on the basis of the laminar steady shear flow model predictions, albeit the shear flow that is established in the shear sublayer next to the wall is neither laminar nor steady in time. For brevity, we leave such a correction out of the reported calculations here, all of which are therefore reported in terms of zero shear rate quantities except for the drag reduction where those corrections can be both important and essential for an accurate estimation (see Section 1.4.1).

Equations (1.1) and (1.2) are not closed because of the presence of the extra stress tensor $\underline{\underline{\tau}}$. Therefore, one more equation is required, which is provided by a viscoelastic constitutive model [35, 49, 79]. According to nonequilibrium thermodynamics, the most thermodynamically consistent way to describe the constitutive model is in terms of internal (structural) variables for which separate evolution equations are to be described [49]. The simplest case is when a single, second-order

and positive definite, tensor, the conformation tensor, $\underline{\underline{c}}$, is used. In that case, the most general constitutive equation is given, in dimensionless form, as [80]

$$\frac{D\underline{\underline{c}}}{Dt} = \underline{\underline{c}} \cdot \underline{\nabla u} + \underline{\nabla u}^{T} \cdot \underline{\underline{c}} + \underline{\underline{g}} + \frac{D_0^+}{Re_{\tau 0}} \underline{\nabla}^2 \underline{\underline{c}}, \tag{1.3}$$

where the superscript T denotes the transpose and $\underline{\underline{g}} = \underline{\underline{g}}(\underline{\underline{c}})$ is a second-order tensor that models the relaxation effects and can be interpreted as a restoring force to equilibrium.

On the right-hand side of the constitutive equation, Eq. (1.3), a diffusion term has been added, as proposed by Sureshkumar and Beris [81], so that in turbulent simulations the high wavenumber contributions of the conformation tensor do not diverge during the numerical integration of this equation in time. This parallels the introduction of a numerical diffusion term in any scalar advection equation (e.g., a concentration equation with negligible molecular diffusion) that is solved along with the flow equations under turbulent conditions [82]. In Eq. (1.3), D_0^+ is the dimensionless numerical diffusivity [54–56]. The issue of the numerical diffusivity is further discussed in Sections 1.3.2 and 1.4.3.

For the cases considered here, the relaxation term $\underline{\underline{g}}$ simplifies into the following expression:

$$\underline{\underline{g}} = -\underline{\underline{\tau}} - \alpha We \underline{\underline{\tau}} \cdot \underline{\underline{\tau}}, \tag{1.4}$$

where the Weissenberg number We is defined as

$$We \equiv \frac{\lambda^* u_\tau^*}{h^*} = \left(\frac{\lambda^* (u_\tau^*)^2}{\nu_0^*} \right) \left(\frac{\nu_0^*}{h^* u_\tau^*} \right) \equiv \frac{We_{\tau 0}}{Re_{\tau 0}},$$

in terms of the zero shear rate friction Weissenberg number, $We_{\tau 0} \equiv \lambda^* ((u_\tau^*)^2 / \nu_0^*)$, and the zero shear rate friction Reynolds number, $Re_{\tau 0}$, where λ^* is the relaxation time of the polymer chains. The polymer extra stress tensor is directly connected to $\underline{\underline{c}}$, through

$$\underline{\underline{\tau}} = \underline{\underline{c}} \cdot \frac{\delta H}{\delta \underline{\underline{c}}}, \tag{1.5}$$

where H is the Hamiltonian (total energy of the system) [49, 80, 83]. For the cases considered here, Eq. (1.5) simplifies in the following dimensionless expression:

$$\underline{\underline{\tau}} = \frac{f(\underline{\underline{c}})\underline{\underline{c}} - \underline{\underline{I}}}{We}. \tag{1.6}$$

The conformation tensor has a definite physical origin and interpretation, typically associated with the second moment of a suitably defined chain end-to-end distribution function [84]

$$\underline{\underline{c}} \equiv \langle \underline{R}\underline{R} \rangle, \tag{1.7}$$

where $\underline{R}$ is the chain end-to-end distance vector. It is important to note here that it is exactly this association that also induces a very special property in the conformation tensor, its positive definiteness. In fact, this property is absolutely essential for its proper interpretation and the thermodynamic consistency (i.e., the requirement of a nonnegative entropy production) of the accompanying evolution equations [49, 83, 85]. Indeed, the eigenvalues of $\underline{\underline{c}}$ and their corresponding eigenvectors have the physical meaning of the square of the average macromolecular size along the primary three directions and the orientation of these directions in space, respectively. More discussion on the implication of the positive definiteness requirements on the numerical methods follows in Section 1.3.2.

When $We \to 0$, then $f \to 1$ and $\underline{\underline{c}} \to \underline{\underline{I}}$, which give that $\underline{\underline{\tau}} = \underline{\nabla v} + (\underline{\nabla v})^{\mathrm{T}}$, and Eqs. (1.1) and (1.2) are reduced to the Navier–Stokes equations. Neglecting the numerical diffusion term and depending on the rheological parameters, α, β_0, and the specific form for function $f = f(\underline{\underline{c}})$, entering Eqs. (1.5), (1.2) and (1.6), respectively, the following well-known constitutive models are recovered:

$$f = 1, \quad a = 0, \quad \beta_0 = 0: \quad \text{Maxwell}, \tag{1.8a}$$

$$f = 1, \quad a = 0, \quad 0 < \beta_0 < 1: \quad \text{Oldroyd-B}, \tag{1.8b}$$

$$f = 1, \quad a > 0, \quad 0 < \beta_0 < 1: \quad \text{Giesekus}, \tag{1.8c}$$

$$f = \frac{L^2 - 3}{L^2 - tr(\underline{\underline{c}})}, \quad a = 0, \quad 0 < \beta_0 < 1: \quad \text{FENE} - \text{P}, \tag{1.8d}$$

where L is the maximum polymer chain extensibility parameter. Note that $f \to 1$ as $L \to \infty$; thus, in this case the FENE-P reduces to the Oldroyd-B model. So far, in DNS of viscoelastic turbulent flows, basically two constitutive models were employed. First, to describe the finite chain length effects in dilute solutions of long flexible macromolecules, the FENE-P model [35, 49, 84] was used. This model arises as an averaging approximation of a microscopic kinetic theory description of the end-to-end distribution of the macromolecular chain deformation with the conformation tensor representing the second moment of that distribution [84]; see Eq. (1.1). Notice that for this model, due to the inherent finite chain extensibility, there is an upper bound for the conformation tensor in addition to its positive definiteness constraint [35]. Second, the network-based Giesekus model [35, 49, 84] has also been used to describe drag-reducing turbulent channel flows of surfactant solutions [19, 65, 66] and viscoelastic effects in concentrated polymer solutions.

Finally, the appropriate boundary conditions are the standard nonslip conditions at the channel walls and periodicity conditions along the homogeneous directions:

$$\underline{u}(x, y = \pm 1, z) = 0, \tag{1.9a}$$

$$\underline{u}, p, \underline{\underline{c}} \text{ periodic in } x,\ z \text{ directions}. \tag{1.9b}$$

No boundary conditions are applied at the walls for the conformation (or the stress) tensor since even in the presence of numerical diffusion, the numerical diffusivity D_0^+ is nonzero only in the bulk; for more details, see Refs [50, 54, 78].

1.3 Numerical Methods for DNS

Outside the spectral method-based DNS work, special mention needs to be made for two finite difference works. First, Min *et al*. [64] used a special upwind finite difference formulation through which they managed to simulate without additional diffusivity for the stress a highly elastic turbulent viscoelastic case (corresponding to Oldroyd-B model) for which maximum drag reduction is obtained. Although the method used has admittedly some distinct advantages over the spectral approach in terms of enhanced stability, one should still be cautious of the fact that the lower order finite difference approximations used in Min's work (as well as in above-mentioned other finite difference works, to a greater extent) also introduce diffusion in the results based on the diffusive character of the finite difference approximations (in Min's work, all approximations are second-order finite differences except for a fourth-order scheme used to approximate the stress divergence term in the momentum equation). Thus, the results of the maximum drag reduction need further independent corroboration.

Second, we need to mention the work by Yu and Kawaguchi [65] that, within a finite difference approximation, employed a special MINMOD finite difference formulation that they demonstrated to be more accurate and more stable than the corresponding formulation that employs an artificial diffusion term. However, it should be noted that since they patterned the value of the numerical diffusivity after the work of Dimitropoulos *et al*. [50], they used significant larger values for it than the ones used in subsequent spectral works [54], also reported here. Yu and Kawaguchi used the Giesekus constitutive model for various flow and rheological parameter values. Whenever those values happen to be close to the ones used in spectral simulations [55], the results are similar. Yu and Kawaguchi [65] also ran simulations at much lower viscosity ratios, corresponding to much higher maximum extensional viscosities, and under these conditions they reported very high drag reductions (more than 70%).

We believe that as far as investigating the large-scale features of turbulence is concerned, lower order approximations are powerful enough, if formulated suitably, to give valuable results. However, we also believe that if one wants to investigate in detail turbulence in many scales of length and time, it is hard to beat the accuracy and efficiency of spectral methods, albeit one has to abide by their limitations in simple geometry applications. Since most of our emphasis is on developing a better understanding of the mechanisms of drag reduction through a detailed investigation of interactions between viscoelasticity and turbulence at multiple scales of length and time, we believe that our primary emphasis on the spectral methods is fully justified.

1.3.1
Spectral Methods: Influence Matrix Formulation

In a fully spectral representation, each primary dependent variable, $S = S(x, y, z, t)$, is approximated through a triple series expansion in terms of its spectral coefficient, $\hat{s}_{rkl} = \hat{s}_{rkl}(t)$. This involves a double Fourier series along the two periodic directions (streamwise and spanwise, using N_x and N_z Fourier modes, respectively) and $N_y + 1$ Chebyshev orthogonal polynomial series along the nonperiodic (shear) direction:

$$S(x,y,z,t) = \sum_{r=-(Nx/2)}^{(Nx/2)-1} \sum_{k=-(Nz/2)}^{(Nz/2)-1} \sum_{l=0}^{Ny} \hat{s}_{rkl}(t) T_l(y) \exp\left\{ 2\pi i \left(\frac{x}{L_x} r + \frac{z}{L_z} k \right) \right\}, \quad (1.10)$$

where the three subscripts "r", "k", and "l" of the generic spectral coefficient $\hat{s}_{rkl}$ are used to denote the corresponding mode in the streamwise, spanwise, and shearwise directions, respectively. The Chebyshev orthogonal polynomials are defined in Refs [86, 87].

The time integration of Eqs. (1.1)–(1.3), where the $\underline{\underline{g}}$ tensor is given by Eq. (1.4) and the stress tensor $\underline{\underline{\tau}}$ by Eq. (1.6), is performed by first formally integrating these equations with respect to time from $t = t_n$ to $t = t_{n+1}$. Then, the following discretized equations are derived:

$$\underline{\nabla} \cdot \underline{u}_{n+1} = 0, \quad (1.11)$$

$$\underline{u}_{n+1} - \underline{u}_n + \int_{t_n}^{t_{n+1}} \underline{u} \cdot \underline{\nabla}\, \underline{u}\, \mathrm{d}t = -\underline{\nabla} p_{\mathrm{eff}} + \frac{\beta_0}{Re_{\tau 0}} \underline{\nabla}^2 \int_{t_n}^{t_{n+1}} \underline{u}\, \mathrm{d}t + \frac{1-\beta_0}{Re_{\tau 0}} \int_{t_n}^{t_{n+1}} \underline{\nabla} \cdot \underline{\underline{\tau}}\, \mathrm{d}t + \Delta t \underline{e}_x, \quad (1.12)$$

$$\underline{\underline{c}}_{n+1} - \underline{\underline{c}}_n = \int_{t_n}^{t_{n+1}} \underline{\underline{F}}\, \mathrm{d}t + \frac{D_0^+}{Re_{\tau 0}} \underline{\nabla}^2 \int_{t_n}^{t_{n+1}} \underline{\underline{c}}\, \mathrm{d}t, \quad (1.13)$$

where $\Delta t = t_{n+1} - t_n$, and, for clarity, we have defined the effective pressure, $p_{\mathrm{eff}} \equiv \int_{t_n}^{t_{n+1}} p\, \mathrm{d}t$, and a second-order tensor: $\underline{\underline{F}} \equiv -\underline{u} \cdot \underline{\nabla}\, \underline{\underline{c}} + \underline{\underline{c}} \cdot \underline{\nabla}\, \underline{u} + \underline{\nabla}\, \underline{u}^{\mathrm{T}} \cdot \underline{\underline{c}} - \underline{\underline{\tau}} - \alpha We \underline{\underline{\tau}} \cdot \underline{\underline{\tau}}$. Note that neither any boundary condition is imposed for the pressure nor any additional approximation is used as in the fractional step method [87, 88]. Instead, to solve for the pressure variable, an iterative approach, the influence matrix or Green's function method, described in Refs [87, 89], is followed.

We describe next two slightly different solution procedures used to find the solution at the time step "$n + 1$".

1.3.1.1 The Semi-Implicit/Explicit Scheme

The first scheme is a classical mixed semi-implicit/explicit scheme [51, 52]. According to this scheme, all linear terms in Eqs. (1.11)–(1.13) are treated implicitly and

nonlinear terms explicitly based on the second-order Adams–Basforth formula:

$$\underline{u}_{n+1}-\underline{u}_n+\frac{\Delta t}{2}(3\underline{u}_n\cdot\underline{\nabla}\,\underline{u}_n-\underline{u}_{n-1}\cdot\underline{\nabla}\,\underline{u}_{n-1})$$
$$=-\underline{\nabla}\,p_{\text{eff}}+\frac{\Delta t\beta_0}{2Re_{\tau 0}}\underline{\nabla}^2(\underline{u}_{n+1}+\underline{u}_n)$$
$$+\frac{\Delta t(1-\beta_0)}{2\text{Re}_{\tau 0}}\underline{\nabla}\cdot(\underline{\underline{\tau}}_{n+1}+\underline{\underline{\tau}}_n)+\Delta t\underline{e}_x, \tag{1.14}$$

$$\underline{\underline{c}}_{n+1}-\underline{\underline{c}}_n=\frac{\Delta t}{2}(3\underline{\underline{F}}_n-\underline{\underline{F}}_{n-1})+\frac{\Delta t\,D_0^+}{2Re_{\tau 0}}\underline{\nabla}^2(\underline{\underline{c}}_{n+1}+\underline{\underline{c}}_n). \tag{1.15}$$

Equation (1.11) remains unchanged. Then, the following steps are used to calculate the required solution at the new time step.

Step 1: The quantity $\underline{\underline{c}}_{n+1/2}=\underline{\underline{c}}_n+\frac{\Delta t}{2}(3\underline{\underline{F}}_n-\underline{\underline{F}}_{n-1})$ is calculated first, and Eq. (1.15) is rearranged as follows:

$$\underline{\nabla}^2(\underline{\underline{c}}_{n+1}+\underline{\underline{c}}_n)-\frac{2Re_{\tau 0}}{\Delta t\,D_0^+}(\underline{\underline{c}}_{n+1}+\underline{\underline{c}}_n)=-\frac{2Re_{\tau 0}}{\Delta t\,D_0^+}(\underline{\underline{c}}_{n+1/2}+\underline{\underline{c}}_n). \tag{1.16}$$

Equation (1.16) is a Helmholtz equation with the unknown sum $\underline{\underline{c}}_{n+1}+\underline{\underline{c}}_n$. This is first transformed in the spectral domain where, due to the separability of the Helmholtz equation, the equations for each pair of Fourier modes (r, k) are fully decoupled with the only coupling appearing among the Chebyshev modes. Thus, by solving the Helmholtz equation with a fast solver [86], the updated solution for the conformation tensor $\underline{\underline{c}}_{n+1}$ is obtained, from which, with the aid of Eq. (1.6), the extra stress tensor $\underline{\underline{\tau}}_{n+1}$ is calculated.

Step 2: By taking the divergence of Eq. (1.13) and demanding the continuity equation, Eq. (1.11), to be satisfied, a Poisson equation for p_{eff} is obtained:

$$\underline{\nabla}^2 p_{\text{eff}}=\underline{\nabla}\cdot\left(-\frac{\Delta t}{2}(3\underline{u}_n\cdot\underline{\nabla}\,\underline{u}_n-\underline{u}_{n-1}\cdot\underline{\nabla}\,\underline{u}_{n-1})+\frac{1-\beta_0}{Re_{\tau 0}}\underline{\nabla}\cdot(\underline{\underline{\tau}}_{n+1}+\underline{\underline{\tau}}_n)\right). \tag{1.17}$$

Equation (1.17) is solved with the same solver as the Helmholtz equation for the conformation tensor by using the influence matrix method [87, 89].

Step 3: The quantity

$$\underline{u}_{n+1/2}=\underline{u}_n-\frac{\Delta t}{2}(3\underline{u}_n\cdot\underline{\nabla}\,\underline{u}_n-\underline{u}_{n-1}\cdot\underline{\nabla}\,\underline{u}_{n-1})$$
$$-\underline{\nabla}\,p_{\text{eff}}+\frac{1-\beta_0}{Re_{\tau 0}}\underline{\nabla}\cdot(\underline{\underline{\tau}}_{n+1}+\underline{\underline{\tau}}_n)+\Delta t\,\underline{e}_x$$

is evaluated first. Then, Eq. (1.14) is rearranged to give another Helmholtz equation for the sum $\underline{u}_{n+1}+\underline{u}_n$:

$$\underline{\nabla}^2(\underline{u}_{n+1}+\underline{u}_n)-\frac{2Re_{\tau 0}}{\Delta t\,\beta_0}(\underline{u}_{n+1}+\underline{u}_n)=-\frac{2Re_{\tau 0}}{\Delta t\,\beta_0}(\underline{u}_{n+1/2}+\underline{u}_n), \tag{1.18}$$

which is solved by using the fast solver and by applying no-slip and no-penetration conditions at the walls. These wall divergence values are all that is needed in order to obtain the correct boundary conditions for the effective pressure by enforcing the requirement that the actual velocity field is divergent free on the boundaries, $\gamma = \pm 1$ (influence matrix technique [47, 89]). This is achieved by considering the final pressure and velocity as the linear superposition of the homogeneous solution and a weighted sum over appropriate Green's functions [47, 89]. The solution of Eq. (1.17) completes the update of all the dependent variables. Then, the same procedure is applied in order to further advance in the next time step.

1.3.1.2 The Fully Implicit Scheme

The fully implicit scheme is based on the second-order accurate Adams–Moulton formulae, that is, at each time step, $n + 1$, all terms (both linear and nonlinear) in Eqs. (1.11)–(1.13) are integrated implicitly as follows:

$$\int_{t=t_n}^{t=t_{n+1}} g(t)\,\mathrm{d}t \approx \frac{\Delta t}{2}(g_n + g_{n+1}), \quad n > 0. \tag{1.19}$$

In this case, Eqs. (1.12) and (1.13) are given as

$$\begin{aligned}\underline{u}_{n+1} - \underline{u}_n + \frac{\Delta t}{2}(\underline{u}_n \cdot \underline{\nabla}\underline{u}_n + \underline{u}_{n+1} \cdot \underline{\nabla}\underline{u}_{n+1}) &= -\underline{\nabla} p_{\mathrm{eff}} \\ &+ \frac{\Delta t \beta_0}{2Re_{\tau 0}} \underline{\nabla}^2(\underline{u}_{n+1} + \underline{u}_n) + \frac{\Delta t(1-\beta_0)}{2Re_{\tau 0}} \underline{\nabla} \cdot (\underline{\underline{\tau}}_{n+1} + \underline{\underline{\tau}}_n) + \Delta t\, \underline{e}_x,\end{aligned} \tag{1.20}$$

$$\underline{\underline{c}}_{n+1} - \underline{\underline{c}}_n = \frac{\Delta t}{2}(\underline{\underline{F}}_n + \underline{\underline{F}}_{n+1}) + \frac{\Delta t\, D_0^+}{2Re_{\tau 0}} \underline{\nabla}^2(\underline{\underline{c}}_{n+1} + \underline{\underline{c}}_n). \tag{1.21}$$

Since the governing equations are nonlinear, the implementation of the implicit algorithm requires an iterative method. A direct iterative scheme based on Newton's method is computationally too demanding. Instead, as an alternative, a predictor-corrector scheme can be used with the corrector to be iteratively applied until a convergence criterion is met. To this end, in Eqs. (1.19) and (1.20) $\underline{u}_{n+1}$, $\underline{\underline{\tau}}_{n+1}$, p_{eff}, and $\underline{\underline{c}}_{n+1}$ are replaced by $\underline{u}_{n+1}^{j+1}$, $\underline{\underline{\tau}}_{n+1}^{j+1}$, p_{eff}^{j+1}, and $\underline{\underline{c}}_{n+1}^{j+1}$, respectively, whenever they appear in a linear way in Eqs. (1.19) and (1.20) and by $\underline{u}_{n+1}^{j}$, $\underline{\underline{\tau}}_{n+1}^{j}$, p_{eff}^{j}, and $\underline{\underline{c}}_{n+1}^{j}$, respectively, whenever they appear in a nonlinear way, where $j = 0, 1, 2, \ldots$. Therefore, Eqs. (1.19) and (1.20) become

$$\begin{aligned}\underline{u}_{n+1}^{j+1} - \underline{u}_n + \frac{\Delta t}{2}(\underline{u}_n \cdot \underline{\nabla}\,\underline{u}_n + \underline{u}_{n+1}^{j} \cdot \underline{\nabla}\,\underline{u}_{n+1}^{j}) \\ = -\underline{\nabla} p_{\mathrm{eff}} + \frac{\Delta t\, \beta_0}{2Re_{\tau 0}} \underline{\nabla}^2(\underline{u}_{n+1}^{j+1} + \underline{u}_n) \\ + \frac{\Delta t(1-\beta_0)}{2Re_{\tau 0}} \underline{\nabla} \cdot (\underline{\underline{\tau}}_{n+1}^{j+1} + \underline{\underline{\tau}}_n) + \Delta t\, \underline{e}_x,\end{aligned} \tag{1.22}$$

$$\underline{\underline{c}}_{n+1}^{j+1}-\underline{\underline{c}}_n=\frac{\Delta t}{2}(\underline{\underline{F}}_n+\underline{\underline{F}}_{n+1}^{j})+\frac{\Delta t\, D_0^+}{2Re_{\tau 0}}\underline{\nabla}^2(\underline{\underline{c}}_{n+1}^{j+1}+\underline{\underline{c}}_n). \tag{1.23}$$

The initial guess for the solution that is required to start the iterative procedure at each time step is obtained either by using a second-order extrapolation scheme, that is, $X_{n+1}^0 \approx 2X_n - X_{n-1}$ where $X = \underline{u}, \underline{\underline{\tau}}, \underline{\underline{c}}$, or by simply applying the semi-implicit/explicit scheme described in Section 1.3.1.1. Note that at each step of the iterative procedure, all nonlinear terms are known. Therefore, a procedure similar to the one described for the semi-implicit/explicit scheme can be applied. It is also worth noting that the last step in the full implicit scheme is the satisfaction of the divergence-free condition, which in spectral space can be enforced to machine accuracy. The implicit use of the continuity in the development of the Poisson equation for the pressure is not enough to guarantee with machine accuracy the satisfaction of the divergence-free condition due to approximation error involved in the solution of the Poisson equation caused by the coupling of the Chebyshev modes. However, the structure and linearity of the continuity equation is such to allow a posteriori correction of the velocity field (in spectral space) so that it is identically satisfied.

The advantage of the full implicit scheme and the direct enforcement of the continuity equation can be more clearly seen when we formulate a suitable Poisson equation for the pressure by taking the divergence of the momentum equation, Eq. (1.2):

$$\underline{\nabla}^2 p=\left(-\frac{\partial(\underline{\nabla}\cdot\underline{u})}{\partial t}+\frac{\beta_0}{Re_{\tau 0}}\underline{\nabla}^2(\underline{\nabla}\cdot\underline{u})\right)+\left(-\underline{\nabla}\cdot(\underline{u}\cdot\underline{\nabla}\,\underline{u})+\frac{1-\beta_0}{Re_{\tau 0}}\underline{\nabla}\cdot(\underline{\nabla}\cdot\underline{\underline{\tau}})\right). \tag{1.24}$$

With the semi-implicit/explicit scheme, the terms in the first parentheses of the right-hand side of Eq. (1.18) are not identically zero. However, with the full implicit scheme in which the continuity equation is satisfied with machine accuracy, these terms are zero and therefore the periodic part of the pressure is more accurately evaluated.

Finally, it should be noted that the spectral coefficient for nonlinear terms can be optionally evaluated using the three half rule for dealiasing along all directions [86]. According to this procedure, and starting from the original $(N_x)\times(N_y+1)\times N_z$ spectral coefficients, all nonlinear terms are evaluated in an extended physical space with $(3N_x/2)\times(3N_y/2+1)\times(3N_z/2)$ points. This is efficiently accomplished by first extending the spectral coefficients, for all dependent variables, by a half in each direction. The additional spectral coefficients are set equal to zero and the extended spectral information is transformed into the extended physical space and all nonlinear terms are evaluated. Then, the results are transformed back into the extended spectral space and are truncated to the original spectral space. The three half rule employed here makes the dealiasing complete (i.e., all the aliasing error is removed) for all quadratic terms and partial for higher order nonlinear terms. In fact, the only partial dealiasing occurs in the calculation of the Peterlin function when the FENE-P model is used (see Eq. (1.6)) since all other nonlinearities are quadratic.

1.3.1.3 Typical Simulation Conditions

Most of the simulation results that are reported in the literature and all those considered here are for zero shear rate friction Reynolds numbers, $Re_{\tau 0}$, 125, 180, 395, and 590. For viscoelastic simulations, the zero shear rate friction Weissenberg number $We_{\tau 0}$ varies from 6 to 125, the viscosity ratio β_0 varies from 0.6 to 0.99, and the Giesekus molecular extensibility parameter α is $1/900$. A typical viscoelastic case, for which many reliable results are available, is $Re_{\tau 0} = 180$, $We_{\tau 0} = 50$, $\beta_0 = 0.9$, and $L = 30$ (when the FENE-P model is used) or $a = 1/900$ (when the Giesekus model is used). In this case, an adequate computational domain to capture all the main turbulent events is $L_x \times L_y \times L_z = 9 \times 2 \times 4.5$, which means that in wall units is $0 \leq x^+ \leq L_x Re_{\tau 0}$, $-Re_{\tau 0} \leq y^+ \leq Re_{\tau 0}$, and $0 \leq z^+ \leq L_z Re_{\tau 0}$. Each dependent variable is approximated by N_x and N_z Fourier modes along the streamwise and spanwise directions, respectively, and $N_y + 1$ Chebyshev polynomials along the shear direction, and for this particular friction Reynolds number and computational domain size, are $N_x \times N_y \times N_z = 96 \times 96 \times 96$. The time step of numerical integration Δt in computational units is 5×10^{-4} for viscoelastic case and 10^{-3} for Newtonian case in the fully implicit method; the semi-implicit and explicit schemes require much smaller Δt, that is, $\Delta t = 2 \times 10^{-4}$ and 5×10^{-4}, respectively.

1.3.2 The Positive Definiteness of the Conformation Tensor

As mentioned above, the conformation tensor $\underline{\underline{c}}$ is a second-order internal structural parameter that has a definite physical origin and interpretation, typically associated with the second moment of a suitably defined chain end-to-end distribution function [84]. It is exactly this association that also induces a very special property in the conformation tensor, its positive definiteness. In fact, this property is absolutely essential for its proper interpretation. The eigenvalues of $\underline{\underline{c}}$ and their corresponding eigenvectors have the physical meaning of the square of the average macromolecular size along the primary three directions and the orientation of those directions in space, respectively. For this physical interpretation to be possible, it is clear that all those eigenvalues need to be positive, that is, that $\underline{\underline{c}}$ is positive definite. This is therefore a property that all models need to preserve and indeed most of them do, provided their corresponding governing equations are exactly solved [49, 90].

However, in numerical simulations of viscoelastic flows the positive definiteness of the conformation tensor can be occasionally lost due to the accumulation of numerical error [54, 55]. Moreover, under these conditions the evolutionarity of the models is not guaranteed [90, 91]. As a consequence, under certain circumstances this can lead to catastrophic Hadamard instabilities [90]. It is therefore advantageous if a general way existed to guarantee the preservation of the positive definiteness in numerical simulations. This is not dissimilar to concentration profile calculations where the nonnegative character of various concentration variables is an essential feature to allow a physical interpretation of the results. Indeed, various techniques have been proposed to circumvent the numerical loss of nonnegativeness, most often through the use of an exponential mapping [92]. However, the development of the

exponential mapping here is a more delicate situation due to the tensorial character of the conformation tensor.

Upwind techniques can and have been developed that preserve the positive definiteness and simultaneously do the smoothing of high frequencies [64, 65]. However, their application is restricted to low-order finite difference schemes. For higher order schemes, such as spectral methods, the only alternative to achieve the necessary smoothing is the explicit addition of artificial numerical diffusion. This idea was first developed by Crochet and coworkers [93, 94] with regard to laminar viscoelastic flows where the equivalence of artificial diffusion to upwind approximations was demonstrated. It was further utilized in a spectral method developed by Sureshkumar and Beris [95] for viscoelastic turbulent simulations. A drawback of the latter method is that its application may destroy the positive definiteness of the conformation tensor. In addition, the conformation tensor can grow beyond its physical bounds. Although these aphysical results appear typically in a small fraction of the computational domain, they still hinder the physical interpretation and cast doubt on the accuracy of the results. However, other alternatives exist, as discussed in the following.

Indeed, new variable representations have recently been developed [41, 96–98] that explicitly avoid the loss of positive definiteness of the conformation tensor. Vaithianathan and Collins [41] use either a continuous eigen decomposition of the conformation tensor (which, when used to numerically solve for eigenvalues, may require an occasional corrective action so that all eigenvalues of C are nonnegative) or a Cholesky decomposition $\underline{\underline{c}} = \underline{\underline{L}} \cdot \underline{\underline{L}}^{\mathrm{T}}$ that automatically guarantees by construction that when one numerically follows $\underline{\underline{L}}$, and for any value of $\underline{\underline{L}}$, $\underline{\underline{c}}$ will retain its positive definiteness. Explicit ways of constructing equations for new variables and implementing their numerical solution were also given. This scheme allowed the solution to be obtained in homogeneous viscoelastic turbulence up to high *We* numbers, the spectra though showed a sharp increase in the magnitude of the high-frequency modes. On the other hand, Fattal and Kupferman [96] proposed an exponential decomposition, $\underline{\underline{c}} = \exp(\underline{\underline{A}})$, so that, again, when one numerically follows the evolution of $\underline{\underline{A}}$ (which is the logarithm of $\underline{\underline{c}}$) and for any value of $\underline{\underline{A}}$, the corresponding $\underline{\underline{c}}$ remains positive definite. Also, here explicit directions were offered as to how to construct the evolution equation for $\underline{\underline{A}}$.

So far, this approach has been followed in several works. We here note only the first two. The first is a finite difference simulation of the lid-driven flow of an Oldroyd-B fluid for which the results appeared convergent up to $We = 2$ with the appearance of oscillations at higher *We* values [97]. The second work concerns the finite element simulation of the flow of a viscoelastic fluid past a cylinder using either an Oldroyd-B or a Giesekus model [49]; convergence results were obtained up to a higher *We* number than before. The convergence is ultimately limited only because of artifacts of the model (in the case of Oldroyd-B) or lack of sufficient resolution to resolve the small scales of the Giesekus model. Either one of these techniques is promising in making spectral (and other macroscopic) simulations equally compatible with hybrid micro–macro simulations as far as the capability of either method to produce physical results is concerned. In addition, adopting the simpler exponential representation

for the conformation tensor of Fattal and Kupferman [96], Housiadas *et al.* [99] have developed a simpler mapping that offers numerical advantages. This most recent idea is based on the Cayley–Hamilton theorem that is used to analytically relate the conformation tensor $\underline{\underline{c}}$ to its logarithm tensor $\underline{\underline{A}}$. In fact, the process of updating $\underline{\underline{c}}$ employs three simple successive mappings, each one of which is introduced to preserve a specific property of $\underline{\underline{c}}$: its boundness, its positive definiteness, and (for computational convenience) the avoidance of underflow or overflow error in calculations. Although the method has already produced promising full DNS results [99], more work is required to improve its computational efficiency before it can see more widespread utilization. The most important outcome so far is the verification of previous DNS spectral results without the drawback of any physical violations on the conformation tensor.

1.4
Effects of Flow, Rheological, and Numerical Parameters on DNS of Turbulent Channel Flow of Dilute Polymer Solutions

1.4.1
Drag Reduction Evaluation

One of the most significant quantities to be evaluated in viscoelastic turbulent flow simulations is undoubtedly the achieved drag reduction [47, 54, 78]. The drag reduction is properly defined on the basis of the ratio of the drag observed after the introduction of the polymer additives versus the drag obtained with pure solvent, while keeping the same bulk Reynolds number [34], taking into account that all transitional effects are eliminated so that to avoid miscounting for drag reduction changes, if any, occurring related to the onset of turbulence [14] are determined as [78]

$$\mathrm{DR} = 1 - \left(\frac{Re_\tau^{(\mathrm{visc})}}{Re_\tau^{(\mathrm{Newt})}} \right)^2_{Re_b}, \tag{1.25}$$

where the bulk Reynolds number Re_b is defined in terms of the average streamwise velocities $\bar{v}^*_{av}$ and the wall shear rate (effective) kinematic viscosity ν^* as $Re_b \equiv (2h^*\bar{v}^*_{av}/\nu^*)$. Now, when the viscoelastic system resulting from the addition of polymers to the Newtonian solvent is really very dilute, the bulk shear viscosity hardly changes, and the bulk Reynolds numbers in both cases (the viscoelastic and the Newtonian one) are simply proportional to the bulk (average) flow velocity; keeping that constant while one measures the pressure drop is therefore sufficient for a drag reduction measurement. In reality though, we do have changes in the effective solution viscosity, and these changes need to be taken into account when calculating the bulk Reynolds number. However, still this effect is typically low.

Most importantly for computational viscoelastic fluid mechanics, most of the channel DNS calculations are not performed for a constant flux (which would have naturally resulted in a constant bulk Reynolds number) but for a constant pressure drop per unit length that results in a constant zero shear rate friction Reynolds number. These runs lead to substantial variations in the (instantaneous and average) bulk Reynolds number from which the drag reduction needs to be estimated. Knowing roughly the relationship between the friction and the average bulk Reynolds number for a Newtonian fluid (from the experimentally determined and DNS confirmed empirical relationships for the skin friction factor – see, for example, Ref. [34]), one can extract such a relationship that also takes into account the already mentioned (in Section 1.2) shear thinning effect in association with viscoelastic results [78].

The final expression, relying on the average streamwise velocities $\bar{v}_{av}^{(visc)}$ and $\bar{v}_{av}^{(Newt)}$ evaluated from the viscoelastic and the Newtonian simulations, respectively, at the same $Re_{\tau 0}$, is given [78] as

$$\mathrm{DR} = 1-\mu_w^{2(1-n)/n}\left(\frac{\bar{v}_{av}^{(visc)}}{\bar{v}_{av}^{(Newt)}}\right)_{Re_{\tau 0}}^{-2/n} = 1-\mu_w^{-2}\left(\frac{Re_b^{(visc)}}{Re_b^{(Newt)}}\right)_{Re_{\tau 0}}^{-2/n}, \quad n \approx 1.14775, \tag{1.26}$$

where

$$\mu_w = \frac{\beta_0}{1+\dfrac{1-\beta_0}{2Re_{\tau 0}}\,\Delta(\bar{\tau}_{xy})} \tag{1.27}$$

and $\Delta(\bar{\tau}_{xy})$ is the average wall shear stress at the two walls. Note that for the Oldroyd-B constitutive model that does not show shear thinning behavior, the mean viscosity ratio at the wall μ_w is 1. By an overbar, we denote x, z, and time-averaged quantities:

$$\bar{g} \equiv \frac{1}{L_x L_z T_f}\int_{x=0}^{x=L_x}\int_{z=0}^{z=L_z}\int_{t=t_0}^{t=t_0+T_f} g(x,y,z,t)\,\mathrm{d}x\,\mathrm{d}z\,\mathrm{d}t, \tag{1.28}$$

where t_0 is the required integration time to reach stationary state (beyond which the statistics are taken), T_f is the integration time in stationary state, and Δ denotes the difference of the measured values at the two walls, $\Delta(\bullet) = (\bullet)_{\text{top wall}} - (\bullet)_{\text{bottom wall}}$, used in order to average the wall results for antisymmetric quantities such as τ_{xy}. For dilute systems, μ_w can be very well approximated by considering the steady-state simple shear flow model predictions corresponding to the average wall shear rate [55, 56, 78]. Equation (1.26) describes the drag reduction for runs performed at constant zero shear rate friction Reynolds number, while Eq. (1.25) describes the drag reduction when the bulk Reynolds number is kept constant. Note that this means that if the flux is the quantity that is instead maintained constant between runs, there is a corresponding correction that also needs to be implemented to accommodate potential viscosity changes.

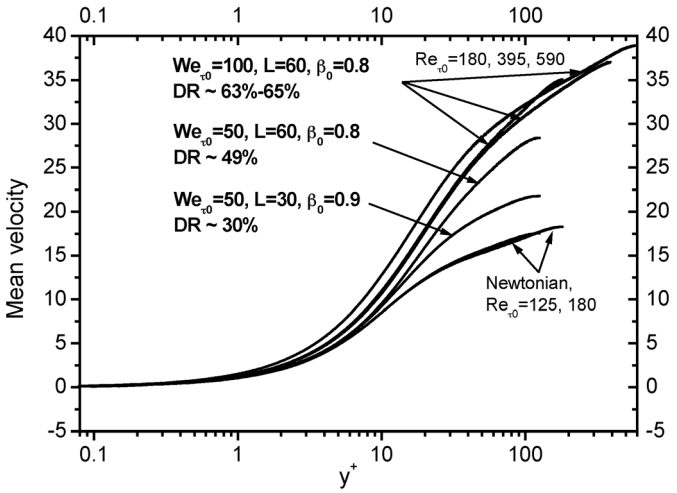

Figure 1.2 DNS results for the mean velocity profiles, obtained for various parameter values of the FENE-P constitutive model, the Newtonian representing the pure viscous solvent base case. (Adapted from Ref. [56].)

1.4.2
Effects of Flow and Rheological Parameters

From our computational viscoelastic DNS work and others (see, for example, Ref. [66]), a rich information has been accumulated concerning the effects that various rheological and flow parameters have on key turbulence statistics and the drag reduction. We will like to present here, drawing from our own work for convenience, some indicative results that we believe have especially led us to improve our understanding of the polymer-induced drag reduction. First, in Figure 1.2, we have collected some representative data on the mean streamline velocity profiles corresponding to a variety of models and model parameter values. It is reassuring to see there that the numerical results look very similar to the experimental data sample presented in Figure 1.1. More specifically, we see in Figure 1.2 that under conditions little departing from the Newtonian reference case (i.e., corresponding to either small Weissenberg number or small extensional parameter L, and/or small polymer concentration that is proportional to $1-\beta_0$), we have a small departure from the Newtonian turbulent results, consisting of a simple parallel translation to higher values of the log linear law segment, in agreement with experimental results [23]. In contrast, under conditions corresponding to higher viscoelasticity, we see that the velocity log-law profile moves further away, and eventually even its slope increases, almost reaching the level of Virk's maximum drag reduction asymptote, exactly in parallel to the trends exhibited by the most drag reduction experimental data shown in Figure 1.1. Therefore, we have confirmed here the main experimental finding that with viscoelasticity the shape of the viscous sublayer remains practically unchanged; however, the buffer layer widens and the log-law layer is pushed higher.

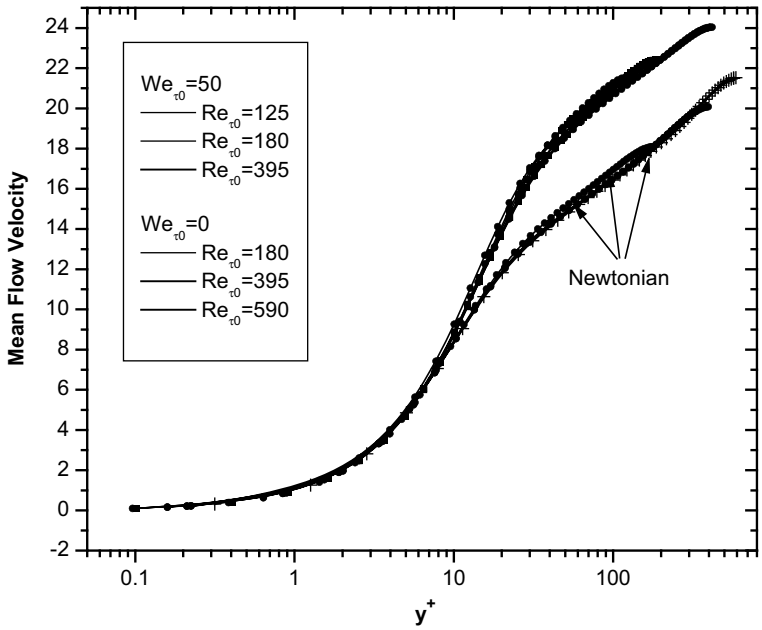

Figure 1.3 Effect of the friction Reynolds number on the mean velocity profile. (Adapted from [54].)

Already in Figure 1.2, by comparing results collected at various Reynolds numbers, we can see that the effect of the Reynolds number, as far as the mean velocity profile (and therefore the drag reduction) is concerned, is minimal. We can also see that even more clearly in Figure 1.3, where results have been collected for fixed rheological parameters (corresponding to a moderate drag reduction case, calculated with the FENE-P model) and at different friction Reynolds numbers. We see that the primary effect of increasing the friction Reynolds number is to be able to allow the log-linear layer to develop more, as well as to push further from the wall as small downturn on the profile that can be attributed to a centerline effect. Note that exactly similar behavior is obtained with Newtonian DNS, also reported in the same figure for comparison purposes. Needless to say those Newtonian DNS results, collected with the same code as in the viscoelastic case, are in perfect agreement with the literature [100].

The effect of the Reynolds and Weissenberg numbers on drag reduction can be most clearly seen in Figure 1.4, where we present the Weissenberg number dependence of the drag reduction, calculated according to the expressions provided in Section 1.4.1. The various curves in Figure 1.4 correspond to different combinations of other rheological parameters and the friction Reynolds number, as indicated in that figure. First, it is important to note that for the range of Reynolds numbers considered, there is minimal, if any, effect that they have on drag reduction. In fact, this parallels what we saw in Figures 1.2 and 1.3 before. As it turns out, one will have

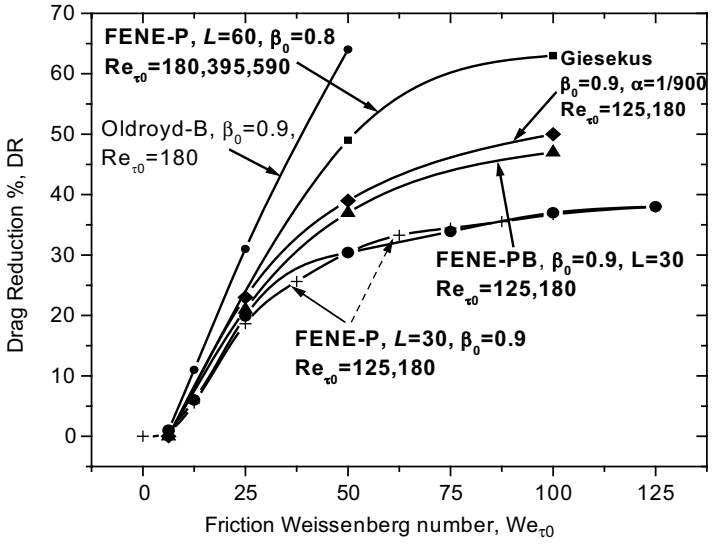

Figure 1.4 Drag reduction predictions as a function of *We* for various values of model parameters. (Adapted from [56] and unpublished data.)

to go to higher order turbulent statistics to see a clear Reynolds number effect – see below for an example and Ref. [58] for more details – on the exception, possibly of results obtained at the smallest Reynolds number, $Re_{\tau 0} = 125$, which being very close to the turbulent transition regime (that can change, depending on viscoelasticity) can introduce some bias in calculations. Similar Reynolds effects are also observed with Newtonian fluids based on experimental [101] and DNS [100] data. Thus, we focus here on discussing results obtained at higher $Re_{\tau 0}$, 180 and more.

Second, note that the various curves shown in Figure 1.4, each one corresponding to a different model with all rheological parameters other than the $We_{\tau 0}$ number fixed, are sigmoidal in shape, with all curves exhibiting a clear onset, around $We_{\tau 0} = 6-8$ and saturation for $We_{\tau 0} > 100$. The main difference between the various curves is then just a question of scale, with the scale determined by the maximum drag reduction obtained at saturation in the limit of very high $We_{\tau 0}$. This saturation value appears to be predominantly dictated by the maximum extensional viscosity that is predicted for a steady extensional flow by the corresponding model and model parameter values: the higher the maximum extensional viscosity, the higher the saturation value for DR. Therefore, an extensional viscosity that significantly increases above the Newtonian limit is identified as the most significant prerequisite for additive-induced drag reduction to take place; the higher the extensional viscosity, the higher the effect. This is most appropriately measured by the Trouton ratio, defined as the ratio of the extensional to shear viscosity [79]. This is consistent with the very high values attributed for the Trouton ratio of even dilute drag-reducing polymer solutions [102] also mirrored, although not to the same high levels, by the Trouton ratio of drag-reducing surfactant solution [103]. For the FENE-P, the

maximum extensional viscosity ratio to the shear viscosity is proportional to $(1-\beta_0)L^2$, where β_0 is the ratio of the solvent viscosity to the total solution viscosity and L is the maximum extensibility parameter. Then, the monotonic increase in DR is indeed observed as we change accordingly the relevant parameter values – compare the FENE-P curves in Figure 1.4 corresponding to $L = 30$, $\beta_0 = 0.9$ (low extensional viscosity) and $L = 60$ and $\beta_0 = 0.8$ (high extensional viscosity). However, when the models vary, there are further secondary effects that enter the picture – one of the main results from DNS is the relatively high sensitivity of the results to details of the rheology and the rheological modeling.

A secondary dependency of DR, beyond that on the extensional viscosity and the Trouton ratio, on the particular constitutive model used is to be expected. This is because various other rheological characteristics (e.g., the second normal stress difference in simple shear flow) that may also be important in the mechanisms underlying drag reduction [104] critically depend on the model. Indeed, in Figure 1.4 we note a significant increase in drag reduction as we move from FENE-P ($L = 30$) to Giesekus ($a = 1/900$), even when the maximum extensional viscosity predicted under these conditions from both models is the same. This enhancement of drag reduction with the Giesekus model has also been observed by other investigators [65], and it is consistent with the hypothesis on the effect of second normal stress difference (present only in the Giesekus model) in drag-reducing flows [104].

It is of interest that even smaller differences between the models, for example, only affecting the detail way that the extensional viscosity depends on the extensional rate (at steady state) and/or the time (during transients), without affecting other rheological parameters, such as the second normal stress difference, may also contribute to significant changes in the predicted drag reduction. Such is the case when a variant of the FENE-P model, the FENE-PB, is introduced in the calculations [57]. Note that both the FENE-P and the FENE-PB predict zero second normal stress difference in simple shear flow and for the same L value ($L = 30$ here) the same maximum extensional viscosity [57]. However, the fact that the latter corresponds to a higher steady-state extensional viscosity at intermediate extensional rates reaching the asymptotic maximum value at smaller extensional rates [57], and also corresponds to faster transients, is sufficient to lead to significantly higher drag reductions, almost as high as those observed with the Giesekus model ($a = 1/900$), as seen in Figure 1.4.

Even more striking than the above observations is the fact that additional simulations show that there is also a secondary effect to the flow keeping the same model and the same maximum extensional viscosity! Indeed, when the combination of the L and β_0 parameters is varied in the FENE-P model, in such a way as to keep the maximum extensional viscosity constant, $(1-\beta_0)L^2 = 90$, we still see some changes in the solution and in particular in the drag reduction, as shown in Figure 1.5. As we can see there, the drag reduction seems to significantly increase for small values of the extensibility parameter L, corresponding to smaller values of the solvent ratio, β_0. A possible explanation of this effect can be again the detail way the extensional viscosity responds to intermediate extensional rates at steady state and/or to intermediate times during transients, albeit the differences in this case are much smaller than those seen before between the FENE-PB and the FENE-P cases. This

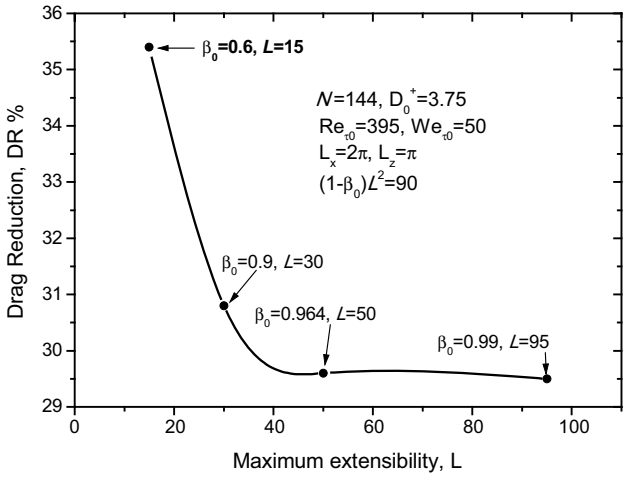

Figure 1.5 Effect of the maximum extensional viscosity to the drag reduction, FENE-P model.

further reinforces our belief that although the extensional viscosity is the primary factor that controls drag reduction, one needs to consider supplemental information in addition to its maximum predicted (saturation) value at infinite extensional rates. This may be explained since despite the fact that typical extensional rates encountered in turbulent DNS are large, they are not infinite, and they definitely vary with time. Thus, it is also important to examine the dependence of the extensional viscosity on the extensional rate and/or time, and the current data seem to support such a view.

Beyond this correlation of model parameters with average macroscopic effects, such as represented by the overall drag reduction, one can find in the detailed numerical results a wealth of additional information. For example, looking at the root mean square of the velocity fluctuation profiles, such as those shown in Figure 1.6, one can clearly see that with increasing viscoelasticity the turbulent velocity fluctuations become more anisotropic. While the rms values of the streamline component increase, those in the shearwise and spanwise directions decrease. The increased anisotropicity has also been confirmed recently through the calculation from DNS of the Lumley anisotropic tensors [105] as has been measured experimentally [106, 107]; it is also interesting to note that this anisotropy tensor information may be used to better understand the drag reduction mechanism [108]. As also seen for Figure 1.6, these changes are accompanied with a clear shift of the streamline rms maximum, typically occurring in the buffer layer, further away from the wall, offering another indication (beyond that seen with the mean streamline profiles in Figure 1.2) of the widening of the wall eddies structures with viscoelasticity. Incidentally, this is also further corroborated by a recent analysis of the large, coherent structures in the flow (eddies) [58, 75].

Form the above DNS findings, it became obvious that the coherence of the large-scale structures is significantly enhanced in the presence of polymer additives. Simultaneously, the eddies become considerably weaker and therefore less capable

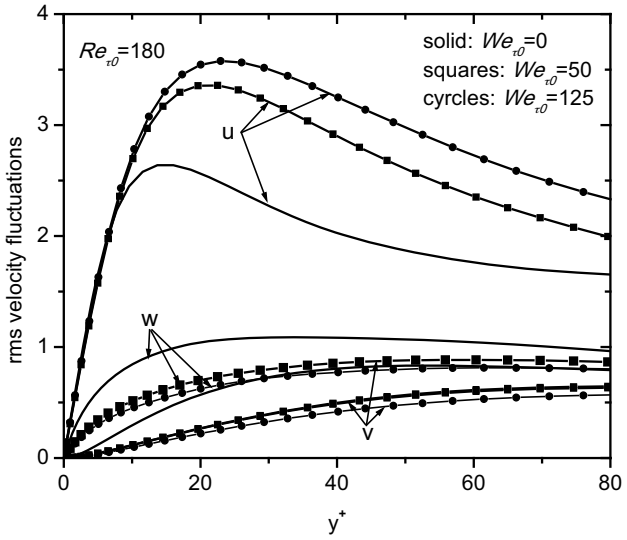

Figure 1.6 The rms velocity fluctuations at friction Reynolds 180. (Adapted from Ref. [54].)

of transferring momentum from the wall. This effect emerges, therefore, naturally as the main mechanism through which turbulence increases drag. This effect has been unequivocally connected through DNS to the enhanced resistance to extension offered by polymer molecules in their stretched state. For example, in Figure 1.7

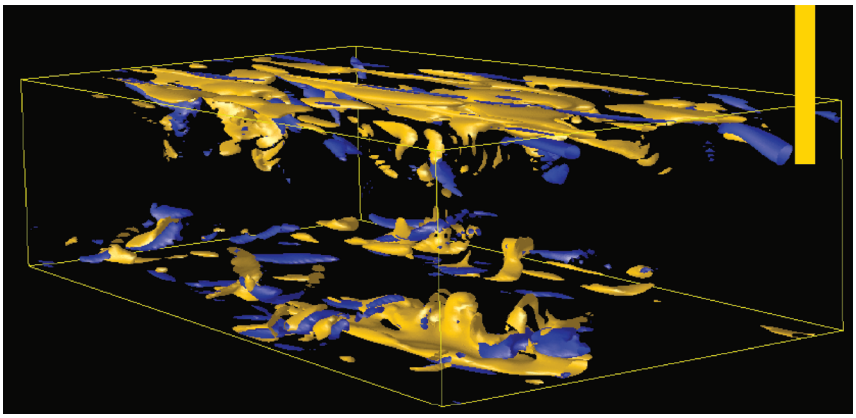

Figure 1.7 Vorticity (with blue) and trace of conformation tensor (with yellow) isosurfaces, close to their maximum values, obtained in a FENE-P polymer simulation of turbulent channel flow. The flow is from back to front with the bottom and top surfaces representing the channel walls. The close-to-maximum vorticity isosurfaces paint the eddies, whereas the close-to-maximum trace of the conformation tensor isosurfaces the location of the most stretched polymer chains in the flow – their close correlation is an indication of the role of the polymers in eddies formation. Alternative rendering of the data also shown in Ref. [58].

we see that the most stretched molecules (as documented from the isosurfaces corresponding to close to the maximum value obtained for the trace of the conformation tensor that can be used to characterize the macromolecular deformation) are to be found near the surface of those eddies (as represented by vorticity isosurfaces at values close to the maximum streamline vorticity). Also, in that figure one can notice the large size of the eddies, much larger than the corresponding Newtonian turbulent channel flow, that closely parallels the increase in the streak spacing also observed in experiments with dilute polymer solutions [23]. In fact, from the first DNS publication [47] it has been noted that the empirically derived linear relationship between the increased streak spacing λ^+ and the drag reduction DR, at small values of drag reduction for dilute polymer solutions [23], $\lambda^+ = 1.9\mathrm{DR} + 99.7$, has also been confirmed from the DNS results [47]. This substantial increase in the streaky structures has also been confirmed in subsequent DNS works with both FENE-P and Giesekus models [50].

The main outcome of the DNS studies has, therefore, been the ample supply of evidence (a small sample of which is provided here) in favor of an extensional viscosity thickening-driven drag reduction mechanism exactly as foreseen by Metzner and coworkers [15] and also independently postulated by Lumley [14]: as the eddies form at the wall, they see with viscoelasticity an increased resistance due to the predominantly extensional character of the velocity deformation and the enhanced resistance to extensional deformation offered by polymers. As a result, the eddies are larger in length, have smaller vorticity values, and are more sluggish; therefore, they become less effective in transferring momentum from the wall, resulting in drag reduction. This is also illustrated in the significantly depressed, by viscoelasticity, values for the streamwise vorticity as seen in Figure 1.8. In the same figure, we see the changes in the vorticity close to the wall because of the changes in the friction Reynolds number. Most of the changes happen when the Reynolds number increases from 125 to 180, then some changes still occur as the Reynolds number increases to 395, from which point there are no perceptible changes as the Reynolds number increases further to 590. The vorticity is one of the quantities most sensitive to Reynolds number change. Figure 1.8 provides evidence that for Reynolds number larger than 395 the results next to wall have converged.

Finally, a very important quantity for determining the wall friction is the Reynolds stress. As numerous DNS studies [47, 54–57, 59, 60, 62–65, 109] have shown, a major viscoelastic effect is a significant lowering in the Reynolds stress in agreement with experimental evidence [22, 23, 25, 26, 62, 110]. In addition, results from a more detailed quadrant analysis have also been reported [58, 111] and show most changes due to viscoelasticity to be concentrated with the fourth and second quadrant events that are found to be significantly decreased in magnitude due to viscoelasticity in the viscous sublayer and the buffer layers, as has been observed experimentally [22, 23]. Furthermore, for a constant friction Reynolds number, we have shown [53, 58] that viscoelasticity is responsible for significantly lowering the production in the Reynolds stresses, in agreement with experiments [23, 48]. A similar decrease is observed in the magnitudes of the terms representing the pressure–velocity gradient correlations, transport, and the overall (viscous and viscoelastic) diffusion and dissipation.

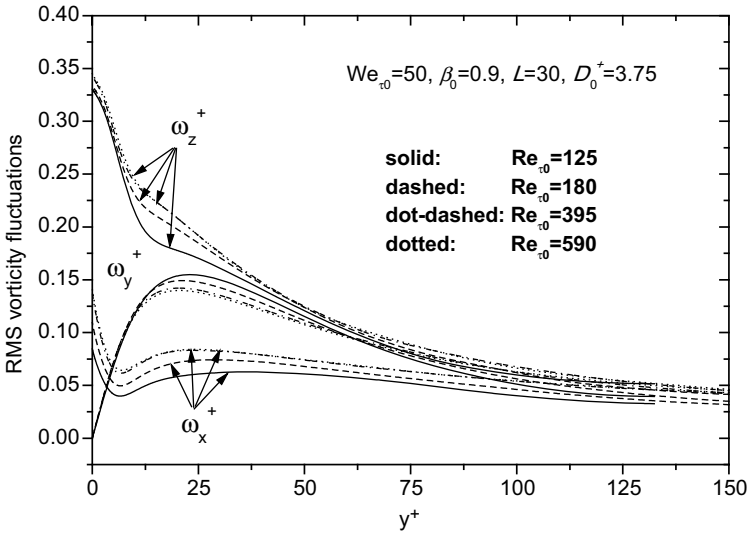

Figure 1.8 Effect of the friction Reynolds number on the vorticity components. (Adapted from Ref. [54].)

Simultaneously, the peaks in the profiles widen and shift toward the centerline. The changes are on the order of 30–70% and are localized in the near-wall boundary layer ($y^+ < 75-100$), leaving the region far away from the wall virtually unaffected. Regarding the terms appearing on the enstrophy budgets, the changes observed due to viscoelasticity are qualitatively similar but much more dramatic in magnitude with reductions of 80–90% being typical. In fact, it is this drastic annihilation of the enstrophy in the wall boundary that may explain the saturation of the drag reduction at a level of about 30–40% obtained with the FENE-P dilute polymer solution constitutive model [58].

1.4.3
Effects of Numerical Parameters

It is important to mention several computational and numerical issues related to the sensitivity of the results to

- time integration scheme;
- different values for the numerical diffusivity;
- different mesh sizes;
- different computational domain sizes;
- long time integration (both in transient and in stationary state).

First, we should comment on the semi-implicit/explicit and fully implicit schemes. The fully implicit scheme gives more physical results and is more accurate and more

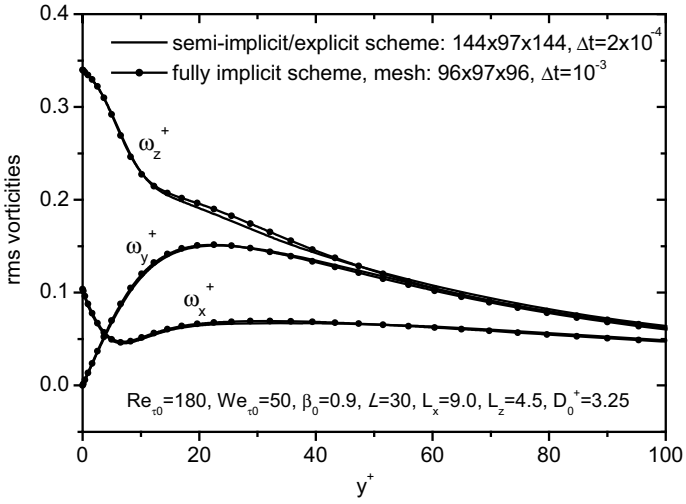

Figure 1.9 Comparison between the semi-implicit/explicit and the fully implicit scheme for the rms vorticity fluctuations. (Adapted from Ref. [55].)

stable allowing considerably larger time steps of integration to be used. On the other hand, it requires both more computational memory and more arithmetic operations per time step. A comparison between these two schemes is offered in Figure 1.9, in which the average vorticity components are given as a function of the distance from the wall. It is clearly seen there that the fully implicit scheme with $\Delta t = 10^{-3}$ and mesh size $96 \times 97 \times 96$ yields the same statistics with the semi-implicit/explicit scheme with $\Delta t = 2 \times 10^{-4}$ and mesh size $144 \times 145 \times 144$.

Second, we present some thoughts about the role of artificial diffusivity in relation to spectral simulations. So far, all indications are that some diffusivity in viscoelastic turbulence simulations is unavoidable (added either explicitly, as is done in spectral methods, or implicitly by using diffusive low-order approximations, such as finite differences, especially when upwind formulations or linearizations in particle Lagrangian formulations [112] are used) as we have seen in all successful simulations of complex viscoelastic flows. Indeed, it is believed that the need to have a conformation diffusion term is the same as the need to add a diffusive term in solving for a passive scalar advection equation in a turbulent flow: it is due to the feature that any chaotic flow field has in creating finer and finer features in the distribution of any passive scalar that it is advected upon its action ([82] and references therein). We stipulate that this is exactly what is happening with the conformation tensor. This becomes even more obvious when one examines the equation for each one of the conformation tensor eigenvalues (Eq. (16) in Ref. [41]) that is exactly like a passive scalar advection equation plus two extra scalar terms, one representing velocity gradient stretching and the other polymer relaxation.

However, the magnitude of the artificial diffusivity has to be kept small, and, when probing convergence of the results with mesh refinement, for consistency,

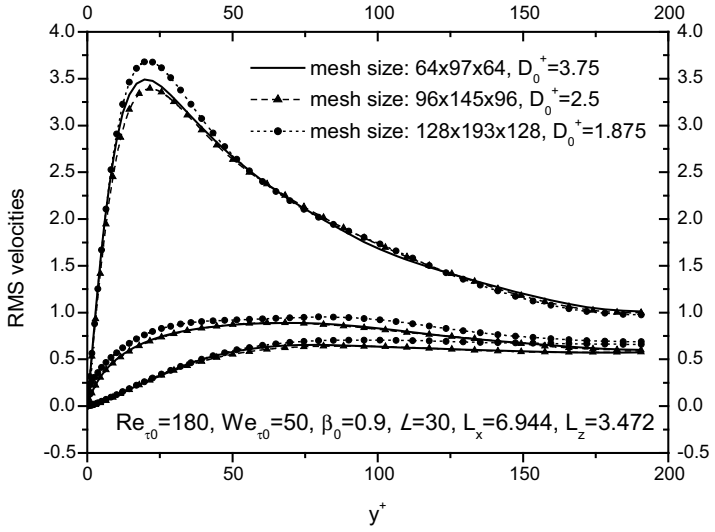

Figure 1.10 Effect of the mesh size and the numerical diffusivity. (Adapted from Ref. [54].)

as the mesh resolution increases, the numerical diffusivity should also decrease. Indeed, this is happening in the convergence study shown in Figure 1.10. The fact that after two successive refinements of the mesh resolution (accompanied by corresponding decreases in the numerical diffusivity) the results for the rms velocities are almost the same is a strong evidence that at least in that case we have reached convergence in the results to a solution independent of the value of the artificial diffusivity. Although every effort has been made in the reported calculations to use diffusivity values that were judged as similarly not altering the physical content of the results, it is to be noted that as the parameter values and/or models change, the role of numerical diffusivity needs to be carefully reexamined. In particular, this is one of the most important factors as extreme range of the parameter values is reached, such as when we approach maximum drag reduction.

In view of the observed enhancement of the larger scales of turbulence by the viscoelasticity of the flow, special attention has also to be paid to viscoelastic simulations to allow a large enough computational domain so that even the larger scales of turbulence can develop. So far, only limited investigations of this effect have been carried out mainly due to the significant computational cost associated with it. Such an example is offered here for the rather small friction Reynolds number 125. In this case, as shown in Figure 1.11, the results obtained after a significant enlargement of the domain by 50% in each direction are almost the same. In this figure, it is interesting to point out another characteristic result arising from the interaction of viscoelasticity with the turbulent flow. In particular, note that the average profile for the trace of the conformation tensor shows a pronounced peak not at the wall (where the maximum shear rates are obtained) but

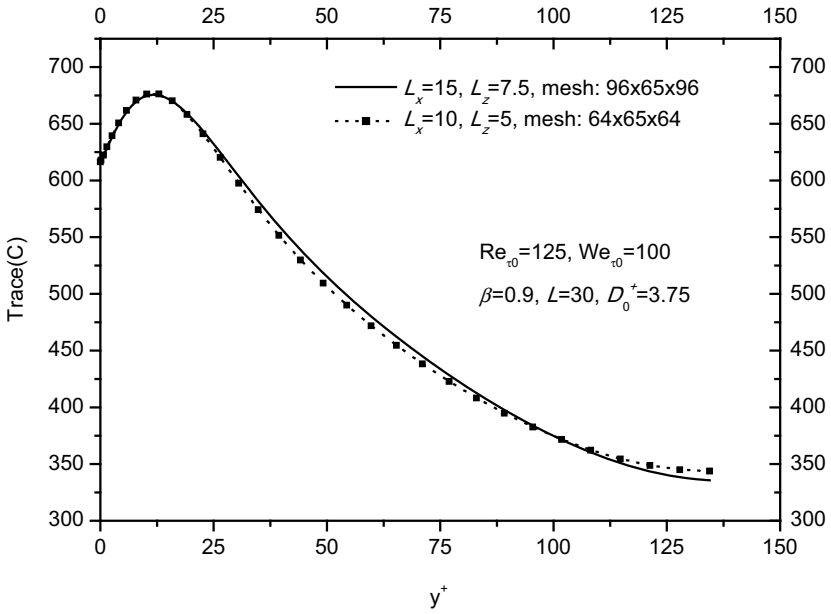

Figure 1.11 Effect of the computational domain.

rather at the beginning of the buffer layer where most of the eddies action takes place. This is a clear indication that the most significant molecular deformation occurs due to the transient extensional characteristics of the flow that accompany the formation of eddies. Note that the issue of identification of the velocity structures that give rise to that pronounced peak in macromolecular deformation (and therefore is critical in the elucidation of details of the drag reduction mechanism) is still a subject of active investigation [105].

1.5 Conclusions and Thoughts on Future Work

We offered in this chapter an overview of some of the most important elements of recent viscoelastic computational work on turbulent channel flow under drag-reducing conditions. After a brief history on the polymer-induced drag reduction phenomenon and presentation of recent computational works, we focused on spectral DNS of turbulent channel flow for dilute polymer solutions. We first presented the governing equations, with emphasis on the two most popular models (FENE-P and Giesekus). Then, we presented the key elements of the spectral method-based numerical algorithms. Following that we discussed in some detail the most important changes to the turbulence induced by viscoelasticity. We can summarize those here as a significant enhancement of the size of the buffer layer, the streamline

velocity fluctuations, and the size of the main eddies that form there, while there is a significant weakening of the streamwise vorticity, and therefore the intensity of the eddies, the Reynolds stress, and the shearwise and spanwise velocity fluctuations. All these were found to contribute to drag reduction through the displacement of the log-law component of the mean streamline velocity profile in agreement with experimental observations. The sensitivity of the above findings to flow and rheological parameters provided significant evidence for the primary role of the extensional viscosity in drag reduction, exactly as originally proposed by Metzner and Lumley.

At present, the numerical simulation activity in this area is focusing on deepening our understanding of the changes induced by viscoelasticity in the structure of turbulence flows. For example, we can mention here the continuing work on the exact coherent states [72], on large-scale structure dynamics through K-L analysis in time [105], and, most recently, on the investigation of the effects of viscoelasticity on small (dissipative) scales of turbulence and intermittency through an analysis of the probability density functions of the velocity and velocity derivatives [113]. These investigations, in addition to further elucidating the underlying mechanism for drag reduction, can also contribute possibly to the development of low-dimensional models of turbulence from first principles. In parallel, as the work to develop various $\varkappa-\varepsilon$-based empirical models of drag reduction [17] is continuing, the DNS data are expected to be further utilized to test those ideas.

Still considerable challenges remain as the strength of viscoelasticity increases and the region of maximum drag reduction is approached due to the very steep computational requirements to evaluate mesh-converged numerical solutions under those conditions. Issues related to polymer inhomogeneities are also important – see, for example, the experimental data of Refs [26, 114] suggesting polymer aggregation and filament formation under conditions of maximum drag reduction. In addition, there is a considerable room for improvement in the development of LES and averaged equations for general viscoelastic turbulent flows, moving beyond channel and pipe flows. One thing is sure that the polymer-induced drag reduction problem is a very challenging one that will keep numerical analysts occupied for a long time.

Acknowledgments

ANB would like to acknowledge the help of the late A.B. Metzner in sharing most of the historical information that appears in the beginning of this work and for the many stimulating discussions and guidance throughout this work. The authors would like to acknowledge the financial support provided by DARPA, Grant No. MDA972-01-1-0007. We are also grateful to the National Center for Supercomputing Applications (NCSA) for providing the computational resources needed for this work through a sequence of NSF-supported supercomputing time allocation grants, the last of which is TG-MCA96N005. Dr. Robert A. Handler and Dr. Gaurab Samanta are also thanked for their contributions. KDH would like to acknowledge the Department of Mathematics, at the University of the Aegean, Greece, for the sabbatical leave of

absence in the fall semester of the academic year 2008–2009 during which this work was done.

References

1 Metzner, A.B. (2004) Turbulent drag reduction. Presentation in a Symposium in Honor of Jan Mewis, Leuven University, Leuven, Belgium, September 22, 2004.

2 Mysels, K.J. (1949) Flow of thickened fluids. US Patent 2,492,173.

3 Toms, B.A. (1949) Some observations on the flow of linear polymer solutions through straight tubes at large Reynolds numbers, in *Proceedings of the International Rheological Congress, Holland, II*, North-Holland, pp. 135–141.

4 Agostan, G.A., Harte, W.H., Hottel, H.C., Klemm, W.A., Mysels, K.J., Pomeroy, H.H., and Thompson, J.M. (1954) Flow of gasoline thickened by Napalm. *Ind. Eng. Chem.*, **46**, 1017–1019.

5 Toms, B.A. (1977) On the early experiments on drag reduction by polymers. *Phys. Fluids*, **20**, S3–S5.

6 Virk, P.S. (1975) Drag reduction fundamentals. *AIChE J.*, **21**, 625–656.

7 Dodge, D.W. and Metzner, A.B. (1959) Turbulent flow of non-Newtonian systems. *AIChE J.*, **5**, 189–203.

8 Fubala, A.G. (1965) The Toms phenomenon in the turbulent flow of very dilute polymer solutions. Proceedings of the 4th International Congress on Rheology, Part 3, pp. 455–479.

9 Metzner, A.B. and Park, M.G., III (1964) Turbulent flow characteristics of viscoelastic fluids. *J. Fluid Mech.*, **20**, 291–303.

10 Hershey, H.C. and Zakin, J.L. (1967) Molecular approach to predicting the onset of drag reduction in the turbulent flow of dilute polymer solutions. *Chem. Eng. Sci.*, **22**, 1847–1857.

11 Castro, W. and Squire, W. (1967) The effect of polymer additives on transition in pipe flow. *Appl. Sci. Res.*, **18**, 81–96.

12 Giles, W.B. and Pettit, W.T. (1967) Stability of dilute viscoelastic flows. *Nature*, **216** (11), 470–472.

13 Virk, P.S., Merrill, E.W., Mickley, H.S., Smith, K.A., and Molo-Christensen, E.L. (1967) The Toms phenomenon: turbulent pipe flow of dilute polymer solutions. *J. Fluid Mech.*, **30**, 305–328.

14 Lumley, J.L. (1969) Drag reduction by additives. *Ann. Rev. Fluid Mech.*, **1**, 367–384.

15 Seyer, A. and Metzner, A.B. (1969) Turbulence phenomena in drag-reducing systems. *AIChE J.*, **15**, 426.

16 Lumley, J.L. and Blossey, P. (1998) Control of turbulence. *Ann. Rev. Fluid Mech.*, **30**, 311–327.

17 Mehrabadi, M.A. and Sadeghy, K. (2008) Simulating drag reduction phenomenon in turbulent pipe flows. *Mech. Res. Commun.*, **35**, 609–613.

18 Zakin, J.L., Lu, B., and Bewersdorff, H.W. (1998) Surfactant drag reduction. *Rev. Chem. Eng.*, **14** (4–5), 253–320.

19 Yu, B. and Kawaguchi, Y. (2003) Effect of Weissenberg number on the flow structure: DNS study of drag reducing flow with surfactant additives. *Int. J. Heat Fluid Trans.*, **24**, 491–499.

20 Zhang, Y., Schmidt, J., Talmon, Y., and Zakin, J.L. (2005) Co-solvent effects on drag reduction, rheological properties and micelle microstructures of cationic surfactants. *J. Colloid Interface Sci.*, **286**, 696–709.

21 Mewis, J. (1974) The rheological properties of suspensions of fibers in Newtonian fluids subjected to extensional deformations. *J. Fluid Mech.*, **62**, 593–600.

22 Luchik, T.S. and Tiederman, W.G. (1988) Turbulent structure in low-concentration drag-reducing channel flows. *J. Fluid Mech.*, **190**, 241–263.

23 Tiederman, W.G. (1990) The effect of dilute polymer solutions on viscous drag and turbulent structure, in *Structure of Turbulence and Drag Reduction* (ed. A. Gyr) Springer, pp. 187–200.

24 Virk, P.S. and Wagger, D.L. (1989) Aspects of mechanisms in Type B drag reduction, in *Structure of Turbulence and Drag Reduction* (ed. A. Gyr) Springer, pp. 201–213.

25 Warholic, M.D., Massah, H., and Hanratty, T.J. (1999) Influence of drag-reducing polymers on turbulence: effects of Reynolds number, concentration and mixing. *Exp. Fluids*, **27**, 461–472.

26 Vlachogiannis, M., Liberatore, M.W., McHugh, A.J., and Hanratty, T.J. (2003) Effectiveness of a drag reducing polymer: relation to molecular weight distribution and structuring. *Phys. Fluids*, **15**, 3786–3794.

27 Sellin, R.H.J. and Moses, R.T. (1984) Proceedings of the International Conference on Drag reduction, Bristol University, Bristol.

28 Sellin, R.H.J. and Moses, R.T. (1989) Drag reduction in fluid flows, in *Proceedings of the IAHR International Conference, Davos*, Ellis Horwood, Chichester.

29 Bushnell, D.M. and Hefner, J.N. (1990) Viscous drag reduction in boundary layers. *Prog. Astronaut. Aeronaut.*, Vol. 123, AIAA, New York.

30 Gyr, A. and Bewersdorff, H.-W. (1995) *Drag Reduction of Turbulent Flows by Additives*, Kluwer Academic Publishers.

31 Nieuwstadt, F. and Den Toonder, J. (2001) Drag reduction by additives: a review, in *Turbulence Structures and Motion* (eds A. Soldati and R. Monti) Springer, New York, pp. 269–316.

32 Graham, M.D. (2004) Drag reduction in turbulent flow of polymer solutions, in *Rheology Reviews 2004* (eds D.M. Binding and K. Walters) The British Society of Rheology, pp. 143–170.

33 White, C.M. and Mungal, M.G. (2008) Mechanics and predictions of turbulent drag reduction with polymer additives. *Annu. Rev. Fluid Mech.*, **40**, 235–56.

34 McComb, W.D. (1990) *The Physics of Fluid Turbulence*, Oxford University Press.

35 Tanner, R.I. (2000) *Engineering Rheology*, 2nd edn, Oxford University Press.

36 Lummus, J.L., Fox, J.E., Jr., and Anderson, D.B. (1961) New low solids polymer mud cuts drilling costs for Pan American. *J. Oil Gas.*, **87**, 1211

37 Burger, E.D., Chorn, L.G., and Perkins, T.K. (1980) Studies of drag reduction conducted over a broad range of pipeline conditions when flowing Prudhoe Bay crude oil. *J. Rheol.*, **24**, 603–626.

38 Alyeska-pipeline (2005) Internet online information at http://www.alyeska-pipe.com/Pipelinefacts/PipelineOperations.html.

39 Lee, W.K., Vaseleski, R.C., and Metzner, A.B. (1974) Turbulent drag reduction in polymeric solutions containing suspended fibers. *AIChE J.*, **20**, 128–133.

40 Hoyt, J.W. (1975) Hydrodynamic drag reduction due to fish slimes. Jn T.Y. Wu, C.J. Brokaw, and C. Brennen (eds.) *Swimming and Flying in nature*, Vol. 2, Plenum Press, New York, pp. 653–672.

41 Vaithianathan, T. and Collins, L.R. (2003) Numerical approach to simulating turbulent flow of a viscoelastic polymer solution. *J. Comput. Phys.*, **187**, 1–23.

42 Dubief, Y., White, C.M., Terrapon, V.E., Shaqfeh, E.S.G., Moin, P., and Lele, S.K. (2004) On the coherent drag-reducing turbulence-enhancing behavior of polymers in wall flows. *J. Fluid Mech.*, **514**, 271–280.

43 Dimitropoulos, C.D., Dubief, Y., Shaqfeh, E.S.G., and Moin, P. (2006) Direct numerical simulations of polymer-induced drag reduction in turbulent boundary layer flow of inhomogeneous polymer solutions. *J. Fluid Mech.*, **566**, 153–166.

44 Den Toonder, J.M., Hulsen, M.A., Kuiken, G.D.C., and Nieuwstadt, F.T.M. (1997) Drag reduction by polymer additives in a turbulent pipe flow: numerical and laboratory experiments. *J. Fluid Mech.*, **337**, 193–231.

45 Orlandi, P. (1995) A tentative approach to the direct simulation of drag reduction by polymers. *J. Non-Newtonian Fluid Mech.*, **60**, 277–301.

46 Wedgewood, L.E. and Bird, R.B. (1988) From molecular models to the solution of flow problems. *Ind. Eng. Chem. Res.*, **27**, 1313–1320.

47 Sureshkumar, R., Beris, A.N., and Handler, R.A. (1997) Direct numerical simulation of the turbulent channel flow of a polymer solution. *Phys. Fluids*, **9**, 743–755.

48 Walker, D.T. and Tiederman, W.G. (1990) Turbulent structure in a channel flow with polymer injection at the wall. *J. Fluid Mech.*, **218**, 377–403.

49 Beris, A.N. and Edwards, B.J. (1994) *Thermodynamics of Flowing Systems*, Oxford University Press, New York.

50 Dimitropoulos, C.D., Sureshkumar, R., and Beris, A.N. (1998) Direct numerical simulation of viscoelastic turbulent channel flow exhibiting drag reduction: effect of the variation of rheological parameters. *J. Non-Newtonian Fluid Mech.*, **79**, 433–468.

51 Orszag, S.A. and Kells, L.C. (1980) Transition to turbulence in plane Poiseuille and plane Couette flow. *J. Fluid Mech.*, **96**, 159–205.

52 Moin, P. and Kim, J. (1980) On the numerical solution of time-dependent viscous incompressible fluid flows involving solid boundaries. *J. Comput. Phys.*, **35**, 381–392.

53 Dimitropoulos, C.D., Sureshkumar, R., Beris, A.N., and Handler, R.A. (2001) Budgets of Reynolds stress, turbulent kinetic energy and vorticity production in the turbulent channel flow of a dilute polymer solution. *Phys. Fluids*, **13**, 1016–1027.

54 Housiadas, K.D. and Beris, A.N. (2003) Polymer-induced drag reduction: effects of the variations in elasticity and inertia in turbulent viscoelastic channel flow. *Phys. Fluids*, **15**, 2369–2384.

55 Housiadas, K.D. and Beris, A.N. (2004) An efficient fully implicit spectral scheme for DNS of turbulent viscoelastic channel flow. *J. Non-Newtonian Fluid Mech.*, **122**, 243–262.

56 Housiadas, K.D. and Beris, A.N. (2005) Direct Numerical Simulations of viscoelastic turbulent channel flows at high drag reduction. *Korea-Aust. Rheol. J.*, **17** (3), 131–140.

57 Housiadas, K.D. and Beris, A.N. (2006) Extensional behavior influence on viscoelastic turbulent channel flow. *J. Non-Newtonian Fluid Mech.*, **140**, 41–56.

58 Housiadas, K.D., Beris, A.N., and Handler, R.A. (2005) Viscoelastic effects on higher order statistics and on coherent structures in turbulent channel flow. *Phys. Fluids*, **17**, 035106, 20 pp.

59 De Angelis, E., Casciola, C.M., and Piva, R. (2002) DNS of wall turbulence: dilute polymers and self-sustaining mechanisms. *Comput. Fluids*, **31**, 495–507.

60 De Angelis, E., Casciola, C.M., L'vov, V.S., Piva, R., and Procaccia, I. (2003) Drag reduction by polymers in turbulent channel flows: energy redistribution between invariant empirical modes. *Phys. Review E*, **67**, 056312 (11).

61 Sibilla, S. and Baron, A. (2002) Polymer stress statistics in the near-wall turbulent flow of a drag-reducing solution. *Phys. Fluids*, **14** (3), 1123–1136.

62 Ptasinski, P.K., Boersma, B.J., Nieuwstadt, F.T.M., Hulsen, M.A., Van den Brule, B.H.A.A., and Hunt, J.C.R. (2003) Turbulent channel flow near maximum drag reduction: simulations, experiments and mechanisms. *J. Fluid Mech.*, **490**, 251–291.

63 Min, T., Yoo, J.Y., Choi, H., and Joseph, D.D. (2003) Drag reduction by polymer additives in a turbulent channel flow. *J. Fluid Mech.*, **486**, 213–238.

64 Min, T., Choi, H., and Yoo, J.Y. (2003) Maximum drag reduction in a turbulent channel flow by polymer additives. *J. Fluid Mech.*, **492**, 91–100.

65 Yu, B. and Kawaguchi, Y. (2004) Direct numerical simulations of viscoelastic drag-reducing flow: a faithful finite difference scheme. *J. Non-Newtonian Fluid Mech.*, **116**, 431–466.

66 Yu, B. and Kawaguchi, Y. (2006) Parametric study of surfactant-induced drag-reduction by DNS. *Int. J. Heat Fluid Trans.*, **27**, 887–894.

67 Zhou, Q. and Akhavan, R. (2003) A comparison of FENE and FENE-P dumbbell and chain models in turbulent flow. *J. Non-Newtonian Fluid Mech.*, **109**, 115–155.

68 Moin, P. and Moser, R.D. (1989) Characteristic eddy decomposition of turbulence in a channel. *J. Fluid Mech.*, **200**, 471–509.

69 Sirovich, L., Ball, K.S., and Keefe, L.R. (1990) Plane waves and structures in turbulent channel flow. *Phys. Fluids A*, **2**, 2217–2226.

70 Sirovich, L., Ball, K.S., and Handler, R.A. (1991) Propagating structures in wall bounded turbulent flow. *Theor. Comput. Fluid Dyn.*, **2**, 307–317.

71 Stone, P.A., Roy, A., Larson, R.G., Waleffe, F., and Graham, M. (2004) Polymer drag reduction in exact coherent structures of plane shear flow. *Phys. Fluids*, **16**, 3470–3482.

72 Li, W. and Graham, M.D. (2007) Polymer induced drag reduction in exact coherent structures of plane Poiseuille flow. *Phys. Fluids*, **19**, 083101. (15 pages).

73 Waleffe, F. (1998) Three-dimensional coherent states in plane shear flows. *Phys. Rev. Lett.*, **81**, 4140–4143.

74 Hof, B., van Doorne, C.W.H., Westerweel, J., Nieuwstadt, F.T.M., Faisst, H., Eckhardt, B., Wedin, H.H., Kerswell, R.R., and Waleffe, F. (2004) Experimental observation of nonlinear traveling waves in turbulent pipe flow. *Science*, **305**, 1594–1598.

75 Handler, R.A., Housiadas, K.D., and Beris, A.N. (2006) Karhunen–Loeve representations of drag reduced turbulent channel flows using the method of snapshots. *Int. J. Numer. Meth. Fluids*, **52**, 1339–1360.

76 Samanta, G., Oxberry, G., Beris, A.N., Handler, R.A., and Housiadas, K.D. (2008) Time-evolution K-L analysis of coherent structures based on DNS of turbulent Newtonian and viscoelastic flows. *J. Turbulence*, **9** (41), 1–25.

77 Pinho, F.T. (2003) A GNF framework for turbulence flow models of drag reducing fluids and proposal for a $\kappa-\varepsilon$ type closure. *J. Non-Newtonian Fluid Mech.*, **114**, 149–184.

78 Housiadas, K.D. and Beris, A.N. (2004) Characteristic scales and drag reduction evaluation in turbulent channel flow of nonconstant viscosity viscoelastic fluids. *Phys. Fluids*, **16**, 1581–1586.

79 Bird, R.B., Armstrong, R.C., and Hassager, O. (1987) *Dynamics of Polymeric Fluids*, vol. **1**, 2nd edn, John Wiley & Sons, Inc., New York.

80 Beris, A.N. (2003) Simple non-equilibrium thermodynamics applications to polymer rheology, in *Rheology Reviews* (eds D.M. Binding and K. Walters), The British Society of Rheology.

81 Sureshkumar, R. and Beris, A.N. (1995) Linear stability analysis of viscoelastic Poiseuille flow using an Arnoldi orthogonalization algorithm. *J. Non-Newtonian Fluid Mech.*, **56**, 151–182.

82 Fox, R.O. (2003) *Computational Models for Turbulent Reacting Flows*, Cambridge University Press, New York.

83 Leonov, A.I. and Prokunin, A.N. (1994) *Nonlinear Phenomena in Flows of Viscoelastic Polymer Fluids*, Springer.

84 Bird, R.B., Curtiss, C.F., Armstrong, R.C., and Hassager, O. (1987) *Dynamics of Polymeric Fluids*, vol. 2, 2nd edn, John Wiley & Sons, Inc., New York.

85 Simhambhatla, M. and Leonov, A.I. (1995) On the rheological modeling of viscoelastic polymer liquids with stable constitutive equations. *Rheol. Acta*, **34**, 259–273.

86 Canuto, C., Houssaini, M.Y., Quarteroni, A., and Zang, T.A. (2006) *Spectral Methods. Fundamentals in Single Domains*, Springer.

87 Deville, M.O., Fischer, P.F., and Mund, E.H. (2002) *High-Order Methods for Incompressible Fluid Flow*, Cambridge University Press.

88 Chorin, A.J. (1968) Numerical solution of the Navier–Stokes equations. *Math. Comput.*, **22**, 745–762.

89 Phillips, T.N. and Soliman, I.M. (1991) The influence matrix technique for the numerical spectral simulation of viscous incompressible flows. *Num. Meth. PDE*, **7**, 9–24.

90 Joseph, D.D. (1990) *Fluid Dynamics of Viscoelastic Liquids*, Springer, New York.

91 Dupret, F. and Marchal, J.M. (1986) Loss of evolution in the flow of viscoelastic fluids. *J. Non-Newtonian Fluid Mech.*, **20**, 143–171.

92 Apostolakis, M.V., Mavrantzas, V.G., and Beris, A.N. (2002) Stress gradient-

induced migration effects in the Taylor–Couette flow of a dilute polymer solution. *J. Non-Newtonian Fluid Mech.*, **102**, 409–445.

93 Crochet, M.J. and Legat, V. (1992) The consistent streamline upwind Petrov–Galerkin method for viscoelastic flow revisited. *J. Non-Newtonian Fluid Mech.*, **42**, 283–299.

94 Marchal, J.M. and Crochet, J.M. (1987) A new mixed finite-element for calculating viscoelastic flow. *J. Non-Newtonian Fluid Mech.*, **26**, 77–114.

95 Sureshkumar, R. and Beris, A.N. (1995) Effect of artificial stress diffusivity on the stability of the numerical calculations and the flow dynamics of time-dependent viscoelastic flows. *J. Non-Newtonian Fluid Mech.*, **60**, 53–80.

96 Fattal, R. and Kupferman, R. (2004) Constitutive laws for the matrix-logarithm of the conformation tensor. *J. Non-Newtonian Fluid Mech.*, **123** (2–3), 281–285.

97 Fattal, R. and Kupferman, R. (2005) Time-dependent simulation of viscoelastic flows at high Weissenberg number using the log-conformation representation. *J. Non-Newtonian Fluid Mech.*, **126** (1), 23–37.

98 Hulsen, M.A., Fattal, R., and Kupferman, R. (2004) Flow of viscoelastic fluids past a cylinder at high Weissenberg number: stabilized simulations using matrix logarithms. *J. Non-Newtonian Fluid Mech.*, **127**, 27–39.

99 Housiadas, K.D., Wang, L., and Beris, A.N. (2010) A new method preserving the positive definiteness of a second order tensor variable in flow simulations with application to viscoelastic turbulence. *Comput. Fluids*, **39**, 225–241.

100 Kim, J., Moin, P., and Moser, R. (1987) Turbulence statistics in fully developed channel flow at low Reynolds number. *J. Fluid Mech.*, **177**, 133–166.

101 Antonia, R.A., Teitel, M., Kim, J., and Browne, L.W.B. (1992) Low-Reynolds-number effects in a fully developed turbulent channel flow. *J. Fluid Mech.*, **236**, 579–605.

102 James, D.F. and Yogachandran, N. (2006) Filament-breaking length: a measure of elasticity in extension. *Rheol. Acta*, **46**, 161–170.

103 Nguyen, H.-P., Ishihara, K., Susuki, H., Kawaguchi, Y., and Usui, H. (2005) Biaxial extensional characteristics of drag-reducing surfactant solution. *J. Soc. Rheol. Jpn.*, **33**, 145–150.

104 Renardy, M. (1995) On the mechanism of drag reduction. *J. Non-Newtonian Fluid Mech.*, **59**, 93–101.

105 Samanta, G., Beris, A.N., Handler, R.A., and Housiadas, K.D. (2009) Velocity and conformation statistics based on reduced Karhunen–Loeve projection data from DNS of viscoelastic turbulent channel flow. *J. Non-Newtonian Fluid Mech.*, **160**, 55–63.

106 Resende, P.R., Escudier, M.P., Presti, F., Pinho, F.T., and Cruz, D.O.A. (2006) Numerical predictions and measurements of Reynolds normal stresses in turbulent pipe flow of polymers. *Int. J. Heat Fluid Flow*, **27**, 204–219.

107 Jovanovic, J., Pashtrapanska, M., Frohnapfel, B., Durst, F., Koskinen, J., and Koskinen, K. (2006) On the mechanism responsible for turbulent drag reduction by dilute addition of high polymers: theory, experiments, simulations, and predictions. *J. Fluids Eng.*, **128**, 118–130.

108 Frohnapfel, B., Lammers, P., Jovanovíc, J., and Durst, F. (2007) Interpretation of the mechanism associated with turbulent drag reduction in terms of anisotropy invariants. *J. Fluid Mech.*, **577**, 457–466.

109 Beris, A.N. and Dimitropoulos, C.D. (1999) Pseudospectral simulation of turbulent viscoelastic channel flow. *Comput. Meth. Appl. Mech. Eng.*, **180** (3–4), 365–392.

110 Kawaguchi, Y., Segawa, T., Feng, Z., and Li, P. (2002) Experimental study on drag-reducing channel flow with surfactant additives: spatial structure of turbulence investigated by PIV system. *Int. J. Heat Fluid Flow*, **23**, 700–709.

111 Kim, K., Li, C.-F., Sureshkumar, R., Balachandar, S., and Adrian, R.J. (2007)

Effects of polymer stresses on eddy structures in drag-reduced turbulent channel flow. *J. Fluid Mech.*, **584**, 281–299.

112 Wapperom, P., Keunings, R., and Legat, V. (2000) The backward-tracking Lagrangian particle method for transient viscoelastic flows. *J. Non-Newtonian Fluid Mech.*, **91**, 273–295.

113 Samanta, G., Housiadas, K.D., Handler, R.A., and Beris, A.N. (2009) Effects of viscoelasticity on the probability density functions in turbulent channel flow. *Phys. Fluids*, **21** article 115106.

114 Shetty, A.M. and Solomon, M.J. (2009) Aggregation in dilute solutions of high molar mass poly(ethylene) oxide and its effect on polymer turbulent drag reduction. *Polymer*, **50**, 261–270.